Journal of Hydrology X 24 (2024) 100180

Contents lists available at ScienceDirect

Journal of Hydrology X

journal homepage: www.sciencedirect.com/journal/journal-of-hydrology-x

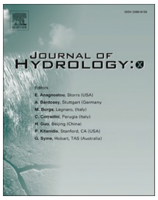

Research papers

# Use of Doppler velocity radars to monitor and predict debris and flood wave velocities and travel times in post-wildfire basins

John W. Fulton [a,*], Nick G. Hall [a], Laura A. Hempel [b], J.J. Gourley [c], Mark F. Henneberg [d], Michael S. Kohn [a], William Famer [e], William H. Asquith [f], Daniel Wasielewski [c], Andrew S. Stecklein [g], Amanullah Mommandi [h], Aziz Khan [h]

[a] *U.S. Geological Survey, Colorado Water Science Center, Denver Federal Center, Lakewood, CO 80225, USA*
[b] *U.S. Geological Survey, Office of Science Quality and Integrity, 201 East 9th St., Pueblo, CO 81003, USA*
[c] *NOAA/National Severe Storms Laboratory, 120 David L Boren Blvd, Norman, OK 73072, USA*
[d] *U.S. Geological Survey Colorado Water Science Center, 445 W Gunnison Ave, Grand Junction, CO 81501, USA*
[e] *U.S. Geological Survey, Integrated Modeling and Prediction Division, Denver Federal Center, Lakewood, CO 80225, USA*
[f] *U.S. Geological Survey, Oklahoma-Texas Water Science Center, Lubbock, TX 79409, USA*
[g] *Colorado Department of Transportation, Region 2 Office, 5615 Wills Blvd., Pueblo, CO 81008, USA*
[h] *Formerly with the Colorado Department of Transportation, USA*

## ARTICLE INFO

*Keywords:*
Doppler velocity radars
Debris and flood wave velocities and travel times
Post-wildfire basins
Flood alert networks

## ABSTRACT

The magnitude and timing of extreme events such as debris and floodflows (collectively referred to as floodflows) in post-wildfire basins are difficult to measure and are even more difficult to predict. To address this challenge, a sensor ensemble consisting of noncontact, ground-based (near-field), Doppler velocity (velocity) and pulsed (stage or gage height) radars, rain gages, and a redundant radio communication network was leveraged to monitor flood wave velocities, to validate travel times, and to compliment observations from NEXRAD weather radar. The sensor ensemble (DEbris and Floodflow Early warNing System, DEFENS) was deployed in Waldo Canyon, Pike National Forest, Colorado, USA, which was burned entirely (100 percent burned) by the Waldo Canyon fire during the summer of 2012 (MTBS, 2020).

Surface velocity, stage, and precipitation time series collected during the DEFENS deployment on 10 August 2015 were used to monitor and predict flood wave velocities and travel times as a function of stream discharge (discharge; streamflow). The 10 August 2015 event exhibited spatial and temporal variations in rainfall intensity and duration that resulted in a discharge equal to 5.01 cubic meters per second ($m^3/s$). Discharge was estimated post-event using a slope-conveyance indirect discharge method and was verified using velocity radars and the probability concept algorithm. Mean flood wave velocities – represented by the kinematic celerity ($c_k = 2.619\,\textit{meters per second},\ \mathrm{m/s} \pm 0.556\,\textit{percent}$) and dynamic celerity ($c_d = 3.533\ \mathrm{m/s} \pm 0.181\,\textit{percent}$)and their uncertainties were computed. L-moments were computed to establish probability density functions (PDFs) and associated statistics for each of the at-a-section hydraulic parameters to serve as a workflow for implementing alert networks in hydrologically similar basins that lack data.

Measured flood wave velocities and travel times agreed well with predicted values. Absolute percent differences between predicted and measured flood wave velocities ranged from 1.6 percent to 49 percent and varied with water slope, hydraulic radius, and depth. The kinematic celerity was a better predictor for steep slopes and wide flood plains associated with the Upper Waldo and Middle Waldo radar streamgages; whereas, the dynamic celerity was a better surrogate for shallow slopes and incised channels such as the Lower Waldo radar streamgage.

The method demonstrates the potential extensibility of a post-wildfire warning system by (1) leveraging multiple systems (i.e., weather radar, near-field velocity and stage radars, and rain gages) for accurate and timely warnings of debris and floodflows, (2) establishing an order of operations to site, install, and operate near-field

---

* Corresponding author.

*E-mail addresses:* jwfulton@usgs.gov (J.W. Fulton), nghall@usgs.gov (N.G. Hall), lhempel@usgs.gov (L.A. Hempel), jj.gourley@noaa.gov (J.J. Gourley), mfhenneb@usgs.gov (M.F. Henneberg), mkohn@usgs.gov (M.S. Kohn), wfarmer@usgs.gov (W. Famer), wasquith@usgs.gov (W.H. Asquith), daniel.wasielewski@noaa.gov (D. Wasielewski), andrew.stecklein@state.co.us (A.S. Stecklein).

https://doi.org/10.1016/j.hydroa.2024.100180
Received 22 January 2024; Received in revised form 18 May 2024; Accepted 27 May 2024

radars and conventional rain gages to record floodflows, forecast travel times, and document geomorphic change in this basin and hydrologically similar basins that lack data, and (3) communicating data operationally with the Colorado Department of Transportation engineering staff, National Weather Service forecasters, and emergency managers.

## 1. Introduction

From 1986 to 2015, floods were responsible for more fatalities in the United States than any other convective weather hazard (Schumacher, 2017). Flood forecasting is particularly challenging in basins affected by wildland fires where flash floods can be dangerous, deadly, and amplified because of post-wildfire conditions (Gourley et al., 2020). Direct runoff is often greater in burned basins and is exacerbated by steep hydraulic grades and hydrophobic soils, which inhibit infiltration, reduce the time of concentration, and increase peak streamflows. Subsequently, the initiation of runoff in response to rainfall can be reduced to minutes, rather than hours, in areas affected by wildland fires, which leaves little time for a proactive response from emergency management agencies and the public. This is particularly true in mountain terrains where spring and summer monsoon events can result in extreme precipitation events, which are difficult to forecast. Monitoring extreme flows in basins altered by wildland fires is difficult, because these basins (1) respond quickly to rain events, (2) are generally not gaged, and (3) are in terrain that restricts access and conventional streamgaging deployments (stage-discharge).

Examples of extreme post-wildfire flood events include the January 2018 flash flood associated with the Thomas Fire, Santa Barbara, California (Lancaster et al., 2021) and the June 2012 Waldo Canyon fire, Colorado (Jarrett, 2013). These events highlight the need to provide accurate and timely monitoring of post-wildfire flood hazards, which tragically resulted in fatalities (Staley et al., 2015). The magnitude and timing of debris and floodflows (collectively referred to as floodflows) in post-wildfire basins can be difficult to measure and are even more difficult to predict. In an attempt to address this challenge, a sensor ensemble consisting of noncontact, ground-based (near-field) Doppler velocity (velocity) and pulsed (stage or gage height) radars, rain gages, and a redundant communication network were deployed to compute flood wave velocities and travel times. To differentiate from satellite or high-altitude platforms, near-field remote sensing is conducted from fixed platforms such as bridges and cable stays. Collectively, this sensor ensemble is branded as the DEbris and Floodflow Early warNing System (DEFENS) and complimented observations from the National Oceanic and Atmospheric Administration's (NOAA) National Weather Service (NWS) NEXRAD weather radar (weather radar).

The objectives of this study are to (1) leverage existing weather radars for advanced floodflow warnings; (2) establish an order of operations to site, install, and operate near-field radars and conventional rain gages to record floodflows and document geomorphic change; (3) operate a redundant communication network to transmit data operationally in post-wildfire basins to decision makers such as the Colorado Department of Transportation (CDOT), the National Oceanic and Atmospheric Administration's (NOAA) National Weather Service (NWS) Weather Forecast Offices (WFOs) and River Forecast Centers (RFCs); and (4) confirm warnings by measuring flood wave velocities at radar streamgages and forecasting travel times to transportation assets such as bridges, culverts, and roads.

## 2. Previous studies

Post-wildfire impacts and extreme weather are compounding events, which can initiate floodflows. Previous collaboration and research conducted in post-wildfire basins provide insight on the thresholds and processes that trigger these events. Each are discussed below.

### 2.1. NWS and USGS collaboration

The NWS and the U.S. Geological Survey (USGS) collaborated in an experimental debris-flow prediction and warning system in the San Francisco Bay area from 1986 to 1995 that relied on forecasts and measurements of precipitation linked to empirical precipitation thresholds to predict the onset of rainfall-triggered debris flows (NOAA-USGS Debris Flow Task Force, 2005). This collaboration provides a basis for the cooperation that was exhibited during this research.

### 2.2. Waldo canyon post-wildfire research

Post-wildfire studies in Waldo Canyon were conducted by Staley et al. (2015), Jarrett (2013), Moore and Park (2012) and Verdin et al. (2012). Staley et al. (2015) established intensity and duration (I-D) thresholds to determine rainfall conditions that could initiate debris flows or flash floods in recently burned areas (Eq. (1)):

$$I = 11.6D^{-0.7} \quad \left(r^2 = 0.99\right) \tag{1}$$

where I is rainfall intensity (millimeter/hour; mm/h), and D is rainfall duration (h) ranging from 0.083 h (5 min; min) to 1 h (Staley et al., 2015). Rainfall I-D thresholds are (1) commonly used to predict the temporal occurrence of debris flows and shallow landslides particularly for storms less than 60 min in duration; and (2) vary based on fine-scale physiographic properties including topography, lithology, soil characteristics, and land cover (Staley et al., 2013; Kean et al., 2011, 2012). Rainfall intensities ranging from 11.6 to 66 mm/h are sufficient to produce debris flows in Waldo Canyon (Staley et al., 2013).

Jarrett (2013) documented peak stream discharge (peak discharge) and rainfall-thresholds required to establish surface runoff in burned areas of Waldo Canyon. Three storms (01 and 10 July and 09 August 2013) were documented by Jarrett (2013). Discharge associated with the 09 August 2013 storm was computed at two locations using indirect methods based on Webb and Jarrett (2002). A maximum rainfall of 35 mm in 35 min (70 mm/h – Upper Williams rain gage; P03) produced a discharge of 50.9 cubic meters per second ($m^3/s$) in the main stem of Waldo Canyon (upstream from the mouth at Waldo Canyon) and 14.2 $m^3/s$ in a tributary to Waldo Canyon. This rainfall threshold exceeds the 66 mm/h threshold prescribed by Staley et al. (2013) responsible for generating runoff.

Moore and Park (2012) prepared a Hydrology Resource Report for the Waldo Canyon fire Burned Area Emergency Response Assessment, which identified risks and proposed measures to protect life, property, natural and critical resources impacted by wildland fires. Post-wildfire risks include human safety threats; debris and floodflows, which could obstruct culverts and overtop roadways; enhanced erosion and deposition; and loss of long-term soil productivity. The estimated recovery period for vegetation regrowth was estimated at 5–7 years (Moore and Park (2012). The land surface is highly dissected by steep channels and banks in the upland, forested portion of the burn. Annual precipitation is comprised of snow during the winter and high-intensity rainstorms during the summer (Moore and Park, 2012).

Verdin et al. (2012) reported a 31 percent, 53 percent, and 63 percent probability of post-fire debris flows in response to precipitation events equal to 29 mm (2-year, 1-h event), 42 mm (10-year, 1-h event), and 48 mm (25-year, 1-h event), respectively.

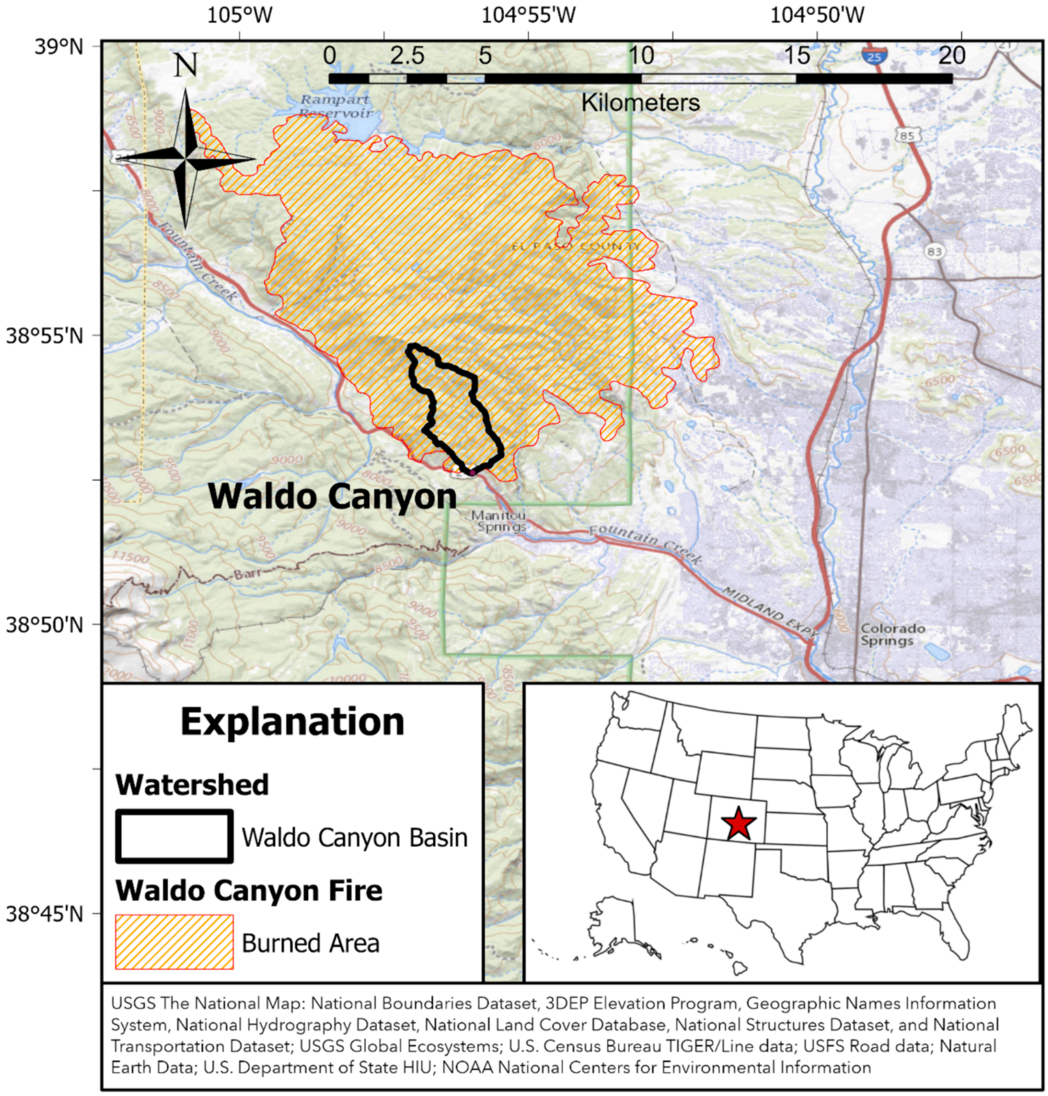

USGS The National Map: National Boundaries Dataset, 3DEP Elevation Program, Geographic Names Information System, National Hydrography Dataset, National Land Cover Database, National Structures Dataset, and National Transportation Dataset; USGS Global Ecosystems; U.S. Census Bureau TIGER/Line data; USFS Road data; Natural Earth Data; U.S. Department of State HIU; NOAA National Centers for Environmental Information

**Fig. 1.** Map illustrating the location of the Waldo Canyon burn scar relative to Waldo Canyon near Colorado Springs, Colorado. Burned perimeter retrieved from Monitoring Trends in Burned Severity (MTBS, 2020).

### *2.3. Weather extremes*

The deadliest and most destructive flash floods generally occur when orographic lift amplifies the intensity and duration of rainfall, which can lead to extreme runoff along steep slopes and canyons (Caracena et al., 1979). Schumacher (2017) emphasized the significance of topography and orographic lift in the formation of extreme rain events and the subsequent hydrologic response. The effects of orographic lift on precipitation intensity are compounded by steep, mountainous terrain that promotes rapid runoff and landslides, particularly in areas denuded of vegetation and duff by wildland fires. Weather forecasts involving heavy rainfall can be inaccurate when precipitation is associated with warm-

**Table 1**

Waldo Canyon basin characteristics, near Manitou Springs, Colorado, USA. [ –[A], not measured or not applicable; Change in elevation divided by length between points 10 and 85 percent of distance along the longest flow path to the basin divides; Mean basin slope computed from 10 m DEM; USGS, U.S. Geological Survey; [1] = USGS (2021a); [2] = USGS, 2023a.]

| Gage type | USGS streamgage name | USGS streamgage identification number [1] | Drainage area (km$^2$) | Basin Characteristics [2] | | |
|---|---|---|---|---|---|---|
| | | | | Mean basin slope (percent) | Mean basin elevation (km) | Elevation change along longest flow path (m/km) |
| Radar streamgage | Waldo Canyon Upper Site near Manitou Springs, CO | 385344104560601 | 1.89 | 43.8 | 2590 | 163.6 |
| Conventional streamgage | Waldo Canyon abv Mouth nr Manitou Springs, CO | 07100750 | 2.62 | 44.7 | –[A] | 150.6 |
| Radar streamgage | Waldo Canyon Middle Site near Manitou Springs, CO | 385309104561101 | 3.29 | 43.8 | 2510 | 143.3 |
| Radar streamgage | Waldo Canyon Lower Site near Manitou Springs, CO | 385254104560401 | 3.68 | 44.7 | 2480 | 134.8 |
| –[A] | Waldo Canyon at US Hwy 24 | –[A] | 4.56 | 45.40 | 2440 | 135.5 |

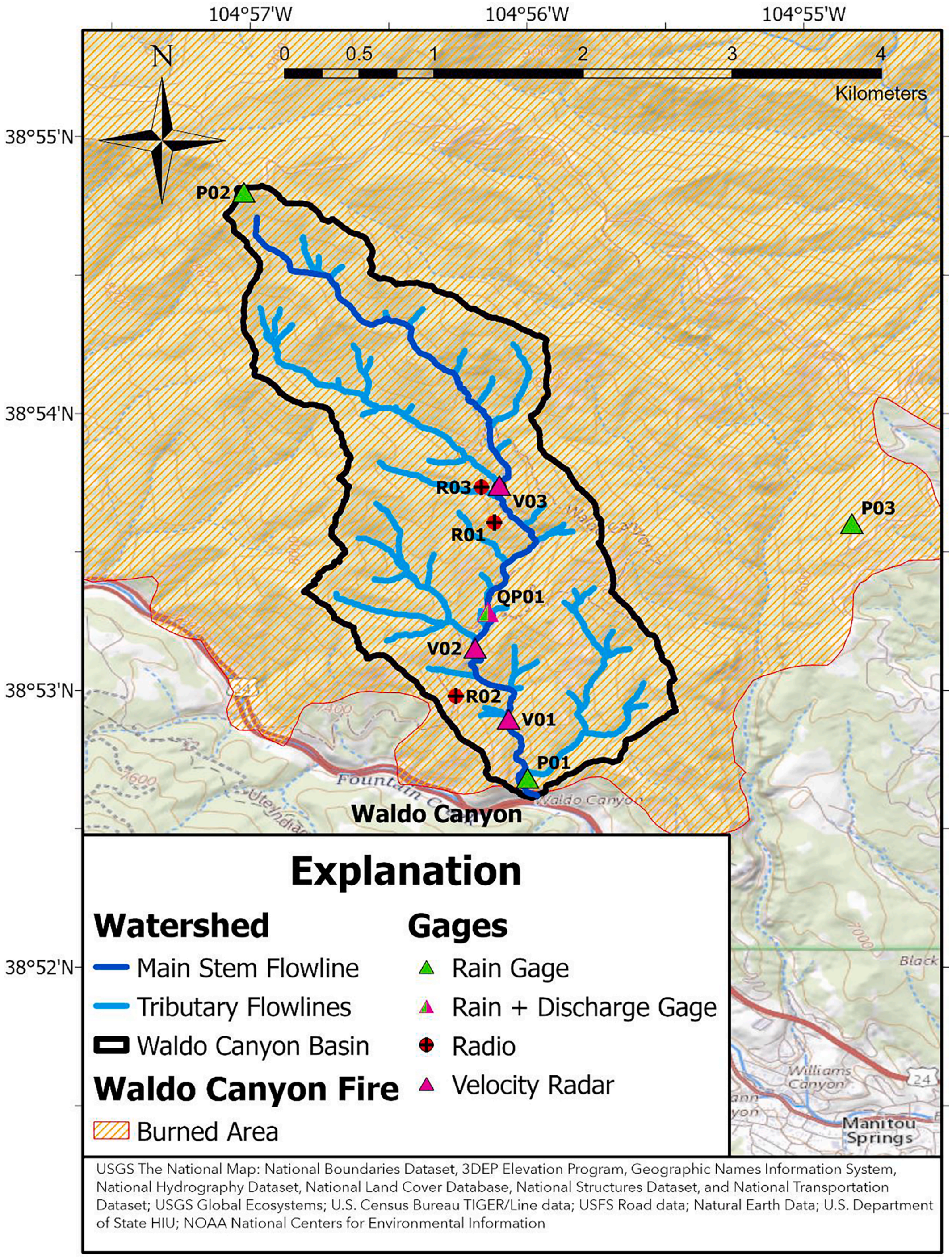

USGS The National Map: National Boundaries Dataset, 3DEP Elevation Program, Geographic Names Information System, National Hydrography Dataset, National Land Cover Database, National Structures Dataset, and National Transportation Dataset; USGS Global Ecosystems; U.S. Census Bureau TIGER/Line data; USFS Road data; Natural Earth Data; U.S. Department of State HIU; NOAA National Centers for Environmental Information

**Fig. 2.** Map illustrating the location of the DEbris and Floodflow Early warNing System (DEFENS), Waldo Canyon near Colorado Springs, Colorado. Burned perimeter retrieved from Monitoring Trends in Burned Severity (MTBS, 2020). Gage locations are described in U.S. Geological Survey (2021a) and Fulton and Hall (2024).

season convection (Shumacher, 2017). Numerical modeling, convection-dominant model forecasts during the warm season (June–August), and quantitative precipitation forecasts (QPF), such as those associated with monsoons, remain a challenge when forecasting precipitation intensity and duration (Fritsch and Carbone, 2004). These factors can result in highly localized and spatially variable rainfall events, which makes runoff prediction and flash-flood forecasting (Barthold et al., 2015) difficult.

### 2.4. *Study area*

During the summer of 2012, the Waldo Canyon fire (Fig. 1) burned the entire basin (18,247 acres), which is undeveloped and located in the Pike National Forest. Approximately 41 percent (7,586 acres) of the burn area was classified as low severity, 40 percent (7,286 acres) was classified as moderate severity, and 19 percent (3,375 acres) was classified as high severity. Of the lands burned, approximately 79 percent (14,422 acres) of the area was located in the National Forest Land, 20 percent (3,678 acres) on private lands, and <1 percent (147 acres) on

**Table 2**

Streamgage and rain gage locations, Waldo Canyon burn scar, [–, not applicable; latitude and longitude referenced as North American Datum of 1983 (2011); USGS; U.S Geological Survey; CO = Colorado; m, meters; USGS, U.S. Geological Survey; $^1$ = USGS (2021a); 2 = Short identifier for USGS gages or radio relays identified in Fig. 2].

| USGS gage identification number $^1$ | Short ID $^2$ | Gage type | USGS gage name $^1$ | Latitude (decimal degrees) | Longitude (decimal degrees) | Flow accumulation (Percent) | Distance from the streamgage to U.S. 24 (m) |
|---|---|---|---|---|---|---|---|
| 385254104560401 | V01 | Radar streamgage | Waldo Canyon Lower Site near Manitou Springs, CO | 38.881669 | −104.934447 | 80.7 | 644 |
| 385309104561101 | V02 | Radar streamgage | Waldo Canyon Middle Site near Manitou Springs, CO | 38.885939 | −104.936461 | 72.2 | 1,460 |
| 385344104560601 | V03 | Radar streamgage | Waldo Canyon Upper Site near Manitou Springs, CO | 38.895558 | −104.935006 | 41.5 | 2,960 |
| 07100750 | QP01 | Rain gage, conventional streamgage | Waldo Canyon above Mouth near Manitou Springs, CO | 38.888111 | −104.935694 | – | 1,786 |
| 385241104560101 | P01 | Rain gage | Lower Waldo Canyon Met above Manitou, CO | 38.878111 | −104.933306 | – | – |
| 385449104565501 | P02 | Rain gage | Upper Waldo Canyon Met above Cascade, CO | 38.913389 | −104.950389 | – | – |
| 385334104544901 | P03 | Rain gage | Upper Williams Canyon Met above Manitou, CO | 38.893444 | −104.913778 | – | – |
| – | R01 | Radio relay | Base station | 38.893423 | −104.935301 | – | – |
| – | R02 | Radio relay | Node station | 38.882980 | −104.937618 | – | – |
| – | R03 | Radio relay | Node station | 38.895558 | −104.935006 | – | – |

Department of Defense lands (Moore and Park, 2012). The geology of the burn area is composed largely of weathered soil associated with the Pikes Peak Granite (Moore and Park, 2012). Prior to the burn, basin vegetation consisted largely of ponderosa pine, mixed conifer, aspen, shrubs, riparian vegetation, and pinyon-juniper (Moore and Park, 2012). Basin characteristics are summarized in Table 1.

## 3. Methods

An effective early-warning system for monitoring hydrologic extremes would deliver a continuum of information regarding the current and forecasted rainfall intensity and duration, as well as the hydrologic response. The first line of defense would rely on rainfall intensity and duration from weather radars. Near-field measurements can improve the accuracy and confidence of post-wildfire flood forecasts. This is particularly important given that Waldo Canyon lies entirely within the burned perimeter of the Waldo Canyon burn scar.

### 3.1. Colorado department of transportation floodflow mitigation initiative

In response to the Waldo Canyon fire, CDOT designed and implemented floodflow mitigation near the mouth of Waldo Canyon and U.S. Highway 24 (U.S. 24) to reduce the risk to the public and CDOT infrastructure. Severe sediment loading at the Waldo Canyon culvert entrance under U.S. 24 was mitigated by constructing a “super” culvert located approximately 1.6 km (km) west of Manitou Springs. The super culvert consisted of a large concrete box culvert (7.3 m (m) wide and 3 m high) and was ten times larger than the original 1.8 m metal pipe used to convey water under U.S. 24. The oversized culvert allowed debris and water to pass under the highway, rather than hydraulically overload or choke the culvert. Upstream from the box culvert, a debris catchment system consisting of a detention basin (to reduce peak discharge) and a GeoBrugg® debris flow barrier (to convey debris and water) was installed. An emergency traffic gate and camera were installed as a precautionary measure in the event floodflows were substantial to overtop U.S. 24.

### 3.2. Waldo burn scar emergency gaging network

In September 2013, the USGS sited and installed a conventional streamgage, tipping-bucket rain gage, and real-time video camera at 07100750 Waldo Canyon above Mouth near Manitou Springs, CO (Waldo Canyon above Mouth; QP01; USGS, 2021a) (Fig. 2, Table 2) to supplement CDOT’s floodflow mitigation initiative. Data were transmitted using GOES satellites. Two additional tipping-bucket rain gages were installed upstream (P02) and downstream (P01) of the conventional streamgage. This early initiative was a flood design project conducted in collaboration with CDOT, El Paso County, U.S. Forest Service, and private-land owners designed to protect and provide safe passage to travelers along U.S. 24 and to monitor extreme runoff and rain events.

### 3.3. DEFENS network design

In May 2015, the DEFENS network was deployed. The network is a sensor ensemble consisting of three velocity and stage radars (V01, V02, and V03), rain gages (P01, P02, and P03), and a redundant communication network (R01, R02, and R03), which operated from May 2015 to October 2016. Real-time surface velocity and stage were transmitted using a redundant communication scheme consisting of two-way cellular (3G) and satellite (Iridium) telemetry (Fig. 2; Table 2). Data were transmitted to USGS and CDOT personnel to monitor the hydrologic response associated with precipitation events. The installation of the radar streamgages augmented the existing infrastructure associated with the September 2013 initiative.

### 3.4. Network siting

It was important to design a network that could capture hydrologic hazards despite variability in rainfall patterns, particularly where rainfall intensity was enhanced by orographic variability. This was addressed by coupling (1) weather radars and (2) near-field velocity and stage radars and rain gages. The near-field radars were operated seasonally from May through October consistent with the monsoon season. Because convective summer storms can be spatially localized over a small area, multiple velocity and stage radars and rain gages were installed to increase the likelihood of capturing runoff events. Subsequently, radar streamgages were sited approximately at subbasin centroids that represented overland flow accumulations of approximately 50, 75, and 100 percent. Attempts were made to collocate radar and rain gages; however, site conditions were limiting. Near-field radar and rain

**Fig. 3.** Image of the deployment of the Lower Waldo radar streamgage, Waldo Canyon near Colorado Springs, Colorado. Photo credit: John Fulton/U.S. Geological Survey.

gage locations are summarized in Table 2.

### 3.5. Network equipment

Because of the lack of infrastructure (bridges and channel walls), Sommer Messtechnik© RQ-30 radars (Fig. 3) were suspended above the streambed using steel cables secured to adjacent trees or bedrock. The Sommer RQ-30 is a fixed-mount, velocity and stage radar. Cable tension was controlled using turnbuckles. Thermal expansion and contraction (Khan et al., 2021) of the cables may have influenced stage measurements and the uncertainty in the stage-area rating (Fulton and Hall, 2024); however, a priority of this research was measuring surface velocities recorded by the velocity radars. Power and data cables were attached to the steel cables and extended bankside to a Pelican® case that housed power equipment (two, 55-amp hour batteries and a solar regulator) and telemetry equipment (cellular and two-way satellite telemetry). Each radar was connected to HyQuest Solutions iRIS 350FX data loggers configured with modems via Serial Device Interface (SDI-12) to provide redundant remote telemetry. The system was powered by solar panels of various wattages (30 W–60 W) depending on location.

Surface velocity, stage, radar spectra quality, battery voltage, and Received Signal Strength Indicator (RSSI) were recorded and transmitted via the communication and telemetry network. The radars were programmed to measure surface velocity and stage every 15 min; however, during extreme events, the measurement frequency was increased to every 1 min based on pre-programmed alarm/notification thresholds. Real-time values were stored in the data loggers for subsequent retrieval by manually downloading the data. The cellular and Iridium-based data loggers at each radar streamgage were programmed to retrieve new data with an offset equal to 30 seconds (s) to avoid data loss between the two data loggers and their embedded modems.

The alarm thresholds for each radar streamgage were based on (1) stage levels that represented 25, 50, 75, and 100 percent of bank-full stage derived from Global Navigation Satellite System (Rydlund and Densmore, 2012) and level surveys (Kenney, 2010) and (2) travel time estimates computed from the mean kinematic celerity and dynamic celerity (collectively referred to as flood wave velocity) based on the surface velocity measured by the velocity radars. In the event alarm thresholds were exceeded, data measurement frequency increased from every 15 min to every 1 min. Data were delivered to USGS personnel via short message service (SMS) text messaging and during extreme events to the Pueblo Colorado NWS WFO, who were responsible for disseminating flash flood warning products.

All three radar streamgages experienced communication challenges due to topographic extremes and canopy shadowing in the incised canyon, which interfered with receiving platforms (cell towers and satellites). Radio relays (line-of-sight radios) consisting of nodes and a base station (Fig. 2) and directional omni directional yagi-antennas were configured to transmit data wirelessly with more reliably. The dual-logger strategy (cellular and two-way satellite telemetry) provided both redundant remote telemetry and alarm notification mechanisms in the event one of the communication protocols failed.

A concerted effort was undertaken to collaborate with representatives from NOAA's National Severe Storms Laboratory (NSSL), NWS Pueblo WFO, and USGS and to notify CDOT staff of impending precipitation events that could trigger floodflows. Flash-flood guidance was established by the NWS Pueblo WFO and relied on NWS weather radar-based rainfall estimates. The USGS near-field sensor ensemble provided ground-based verification of the runoff magnitude and timing to assist CDOT engineering and maintenance staff with monitoring flood wave velocities and travel times associated with extreme hydrologic conditions that could trigger highway shut down protocols. The weather radar operated by NSSL and the NWS Pueblo WFO served as the first line-of-defense when issuing a Watch, Warning, or Advisory.

### 3.6. Order of operations to estimate flood wave velocity and travel time

The order of operations to estimate flood wave velocity and travel time included the following steps: (1) estimate the 10 August 2015 peak discharge based on field measurements from the QP01 gage site, (2) compute at-a-section slope, hydraulic radius, and depth (i.e., hydraulic parameters) associated with the 10 August 2015 peak discharge, based on a pre-existing lidar dataset and Manning's equation, (3) compute uncertainty in the at-a-section hydraulic parameters, (4) compute flood wave velocity and travel time based on findings from steps 1–3, and (5) validate flood wave velocities based on surface velocities measured from velocity radars. Although the methods for computing discharge are well-established, the integration of near-field, real-time velocity and stage radars to validate streamflow in response to extreme precipitation events is unique.

### 3.7. Step 1. Estimate the 10 August 2015 peak discharge

To estimate the peak discharge associated with 10 August 2015 precipitation, two methods were used: (1) slope-conveyance indirect (indirect) discharge computation established at the conventional streamgage (Waldo Canyon above Mouth) and (2) probability concept algorithm. Peak discharge was estimated from data collected at the QP01 gage site and although the precipitation distribution was variable spatially and temporally, the peak discharge was assumed to be constant throughout the basin.

An indirect discharge was computed using the methods prescribed by Bradley (2012), Fulford (1994), and Dalrymple and Benson (1968). Dalrymple and Benson (1968) summarize the slope-area indirect discharge method. Fulford (1994) and Bradley (2012) describe the USGS computer program Slope-Area Computation Graphical User Interface (SACGUI) used to compute the peak discharge as a function of the surveyed cross sections and Manning's *n* assigned to the high-water marks that were previously plotted by SACGUI in the field. The slope-area method is based on uniform flow as a function of channel characteristics, water-surface profiles, and a roughness coefficient (Dalrymple and Benson, 1968). Although the slope-area method is based on a uniform flow, the method applies to one-dimensional, gradually varied, steady-flow equations and uses the conservation of energy and mass and the normal-flow equation to estimate discharge (Chow, 1959; Fulford, 1994).

The probability concept algorithm relies on the surface velocity recorded by the three velocity radars (Fig. 2, Table 2). Surface velocity is translated to a mean velocity using an alternative velocity distribution equation based on the probability concept, which was pioneered by Dr. C.-L. Chiu (Chiu, 1987; Chiu, 1989; Chiu et al., 2001; Chiu and Tung, 2002; Moramarco et al., 2004; Chiu,et al., 2005; Chiu and Hsu, 2006; Fulton and Ostrowski, 2008; Moramarco et al., 2017; Fulton et al., 2020a, Fulton et al., 2020b). By computing $\phi$ and directly measuring $u_{max}$ from the velocity radar, $u_{mean}$ can be estimated using Eq. (2):

$$\phi = u_{mean}/u_{max} \tag{2}$$

The parameter $\phi$ generally ranges from 0.58 to 0.82 (Chiu and Hsu, 2006), and for the purpose of this application, $\phi$ was assumed to equal $0.70 = [(0.58 + 0.82)/2]$, which is consistent with the findings of Fulton et al., (2020a,b). Discharge was computed using Eq. (3) based on the measured $u_{max}$ and the cross-sectional area derived from the stage-area rating (Fulton and Hall, 2024), which was computed using AreaComp3 (USGS, 2021b):

$$Q = \phi \times u_{max} \times A \tag{3}$$

where $Q$ = discharge; $\phi = u_{mean}/u_{max}$; $u_{max}$ = maximum-instream velocity = surface velocity at the y-axis (stationing where $u_{max}$ is coincident with the velocity radar location stationing in the cross section); $A$ = cross-sectional area; $u_{mean}$ = mean velocity. Manning's equation was parameterized using the peak discharge to establish at-a-section hydraulic parameters.

*Step 2. Compute At-a-section Hydraulic Parameters using Manning's Equation*

Because of the spatial variability in at-a-section hydraulic parameters, computing flood wave velocities and travel times in near-real time for a given discharge is untenable using traditional, physically based numerical hydraulic models. Instead, a simplified, more efficient approach based on Manning's equation was used. In this approach, we estimate at-a-section hydraulic parameters associated with the 10 August 2015 peak discharge from step 1 using Manning's equation. Uncertainties in at-a-section hydraulic parameters were then estimated in step 3, and results from steps 1–3 were used to compute flood wave velocity and travel time in step 4. R was used to complete this step over other tools such as widely accessible numerical models because of (1) matter of convenience for the user, particularly if they are not familiar with hydraulic modeling; (2) seamlessness of the R script to derive at-a-section hydraulic parameters and the integration of the R scripts lmomco (Asquith, 2022) and plotlmrdia (Asquith, 2011), which were used in the uncertainty analysis; and (3) transferability to other post-wildfire basins (R Core Team, 2022).

To simplify flood wave velocity calculations, geomorphic characteristics influencing discharge along the main stem Waldo Canyon were summarized based on a lidar-derived Digital Terrain Model (DTM) with 0.6 m pixel resolution, obtained from the USGS 3D Elevation Program (3DEP; USGS, 2021c) and analyzed in ArcGIS (version 10.8.1, ESRI, 2020) and R (version 4.2.2, R Core Team, 2022). A main stem flowline was delineated from the DTM using the built-in *fill, flow direction,* and *flow accumulation* tools in ArcGIS. The main stem flowline and the DTM were exported to R and were used to create 181 evenly spaced cross sections, approximately every 30 m, between the uppermost main stem flowline point near the USGS rain gage 385449104565501 (Upper Waldo Canyon Met above Cascade, CO; USGS, 2021a) and the confluence with Fountain Creek near U.S. 24 (Fig. 2). Each cross-sectional elevation profile, was generated perpendicular to the main stem flowline, was approximately 91 m in length, and was comprised of 150 points spaced evenly every 0.6 m.

The shape of the main stem flowline was irregular and, in some cases, sharp bends led to cross sections that were parallel to the hillslope rather than perpendicular to the flow direction. These linear cross section profiles were not representative of the true stream channel characteristics; cross-sections were considered invalid and were not used in the analysis if the thalweg (i.e., the lowest elevation in the cross-sectional profile) was greater than 6 m from the ArcGIS delineated flowline. Of the 181 cross sections generated, 113 were considered valid.

The cross sections were used to calculate the hydraulic geometry parameters required for maintaining a constant discharge using Manning's equation (Eq. (4)), which calculates uniform flow in open channels. Manning's equation can be expressed as:

$$Q = u_{mean} \bullet A = \left(\frac{1}{n}\right) A \bullet R^{2/3} \sqrt{S} \tag{4}$$

where $Q$ = discharge in cubic meters per second ($m^3/s$), $u_{mean}$ = mean cross section velocity (mean velocity) in meters per second (m/s), $A$ = cross-sectional area of flow in square meters ($m^2$), $n$ = Manning roughness coefficient ($s/m^{1/3}$), $R$ = hydraulic radius in meters (m), and $S$ = channel slope (m/m). Hydraulic radius is defined as:

$$R = \frac{A}{P_w} \tag{5}$$

where $P_w$ = wetted perimeter of the cross section (m). Therefore, by replacing the hydraulic radius in Eq. (4) with Eq. (5), Manning's equation is expressed as Eq. (6):

$$Q = \left(\frac{1}{n}\right)\bullet A^{5/3}\bullet P_w{}^{-2/3}\sqrt{S} \tag{6}$$

Channel bed slope was calculated from the longitudinal elevation profile derived from the main stem flowline. Manning's roughness coefficient ($n$) was assumed constant across all cross sections and did not vary with water depth. Based on the abundance of cobbles and boulders in the existing stream channel and flood plain, severe degree of surface irregularity, variations in cross section shape, appreciable number of obstructions in and near the channel, and moderate levels of vegetation immediately adjacent to the stream channel, $n$ was estimated to be constant at 0.1 at all cross sections based on guidelines published for similar montane environments (Yochum and Bledsoe, 2010). Manning's $n$ is a potential source of error and was assigned an uncertainty equal to 25 percent.

The remaining variables in Eq. (6) – *cross-sectional area (A) and wetted perimeter* ($P_w$) – are dependent on stage. Using R codes, $A$ and $P_w$ values associated with the 10 August 2015 peak discharge were estimated for each cross section based on at-a-section hydraulic geometry relations. Hydraulic geometries ($A$ and $P_w$ values) were calculated by iteratively imposing a range of stage values at each cross section. At each iterative stage, discharge was estimated using Manning's equation (Eq. (6)) parameterized with that iteration's calculated hydraulic geometries; the $A$ and $P_w$, and stage values that yielded the most similar discharge value to the measured 10 August 2015 peak discharge were then used in subsequent analyses. The imposed stage values ranged from a minimum of 0.015 m and a maximum of 1.5 m above the thalweg (i.e., lowest elevation in the cross section), and were analyzed over 0.015 m increments.

Lastly, several additional parameters associated with the 10 August 2015 peak discharge were computed and used in subsequent analyses. At each cross section, Eq. (4) was used to compute $u_{mean}$ and additional at-a-section channel characteristics – *top-width and mean depth* – were calculated using methods similar to those used in AreaComp (USGS, 2021b). The channel characteristics from step 2 were used to compute flood wave velocities and travel times at each of the 113 valid cross sections.

*Step 3. Compute Uncertainty in the At-a-section Hydraulic Parameters.*

Reliability requires information on uncertainty, which is represented by the standard deviation or coefficient of variation (Ang and Tang, 1990). To estimate the kinematic celerity and dynamic celerity, which were assumed to represent flood wave velocities, an uncertainty analysis was conducted using (1) raw at-a-section hydraulic parameters and (2) L-moments derived from the *lmomco* and *plotlmrdia* packages in R (Asquith, 2011).

Raw data associated with the at-a-section hydraulic parameters were leveraged to compute uncertainties based on relevant statistics such as the minimum, mean, median, maximum, standard deviation (s.d.) and coefficient of variation (CV). The raw at-a-section hydraulic parameters represent actuals from Waldo Canyon and offer a direct method for computing flood wave velocities and their uncertainty. In contrast, L-moments represent a model of Waldo Canyon and offer an indirect method for computing flood wave velocities and their uncertainty. This is particularly valuable in basins that lack data on at-a-section of hydraulic parameters. L-moments are used to establish the shape of a probability density function (PDF; Li et al., 2022) and consist of a series of linear combinations of order statistics (L-statistics), which include four L-moments and their associated ratios such as the mean, coefficient of variation, skewness, and kurtosis (Li et al., 2022). L-moment plots of slope, hydraulic radius, and depth were generated using the L-skew and L-kurtosis of 100 sub-samples of the valid cross section population (113 cross sections). Each of the 100 sub-samples was comprised of 71 cross sections (approximately 63 percent of the 113 valid cross sections) randomly selected using the "sample" function in R. The distribution of L-skew and L-kurtosis of the 100 sub-samples were used to determine appropriate PDFs and cumulative density functions (CDFs) to represent distributions of each of the hydraulic parameters (slope, hydraulic radius, and depth).

The total uncertainty in flood wave velocities is described by Eq. (7):

$$\Omega = \sqrt{inherent\ variability^2 + random\ error^2 + systematic\ error^2} \tag{7}$$

$$\Omega = \sqrt{\left(\frac{sample\ s.d.}{sample\ mean}\right)^2 + \left(sample\ s.d.\big/mean\big/\sqrt{no.\ of\ samples}\right)^2}$$

where the total uncertainty consists of (1) inherent variability associated with a physical phenomenon and (2) random errors associated with the predicted values. For the purpose of this research, only random errors are considered. All are expressed in terms of CV. The at-a-section hydraulic parameters represent the nominal geomorphic characteristics of the 113 cross sections and do not account for change that may occur between the cross sections.

*Step 4. Compute Flood wave Velocity and Travel Time.*

Flood wave velocities can be indirectly computed relative to the ambient mean velocity that was calculated from the modified Manning's equation (Eq. (6)) in steps 1–3. Chow et al. (1988) discuss two terms used to estimate flood wave velocities: kinematic and dynamic celerity. Kinematic celerity ($c_k$) is expressed in terms of depth and slope. The solution for the kinematic celerity in prismatic channels (square or rectangular), based on Manning's equation and the Chezy equation (Chow, 1959), is summarized in Eqs. (8) and (9), respectively.

$$c_k = \frac{1}{B}\frac{d}{dy}\left(\frac{1}{n}S_0^{1/2}(By)y^{2/3}\right) = \left(\frac{1}{n}S_0^{1/2}\left(\frac{5}{3}\right)y^{2/3}\right) \tag{8}$$

where $Q =$ discharge, $n =$ Manning's n, $S_f = S_0$, $A =$ channel area, $y =$ channel depth, $B =$ top width. Dynamic celerity ($c_d$) is expressed as (Chow et al., 1988):

$$c_d = \sqrt{gy} \tag{9}$$

where $g = gravitational\ constant, \frac{m}{s^2}$. The flood wave velocity derived from the surface velocity recorded by the velocity radars in the downstream direction equals $u_{mean} + c_d$.

Flood wave travel times were estimated using the centerline stream distance from the radar streamgages to U.S. 24 (Table 2) divided by the mean values of the kinematic celerity and dynamic celerity, which were derived for prismatic channels and computed based on at-a-section hydraulic parameters associated with the 10 Aug 2015 peak discharge.

*Step 5. Validate Flood wave Velocities based on Surface Velocities measured from Velocity Radars.*

Flood wave velocities were computed and compared to the radar-derived surface velocities recorded during the 10 August 2015 event. The three velocity and stage radars were installed in June 2015 prior to the monsoon season and used to measure surface water velocities and provide a platform for validating the computed kinematic celerity and dynamic celerity.

## 4. Results

Findings from this research demonstrate that instantaneous surface velocity, stage, and precipitation data can be delivered in real-time, resulting in quicker response times and enhanced actions to maintain public safety and transportation infrastructure. This can be particularly important in areas where long-term streamgages do not exist or where they do exist and are not intentionally operated as a warning system application. An effective early-warning system for monitoring hydrologic extremes delivers a continuum of information regarding current and forecasted rainfall intensity and duration, as well as the hydrologic response. The first line-of-defense often relies on rainfall intensity and duration from weather radars. This metric offers the greatest lead time to prepare for weather extremes and may be guided by an Intensity-Duration (I-D) threshold (Staley et al., 2015; Cannon et al., 2011;

**Table 3**
August 10, 2015 precipitation data recorded by rain gages, Waldo Canyon near Colorado Springs, Colorado, USA reported in U.S. Geological Survey (2021a), [–, not measured or not applicable].

| Station name and number | | | | | | |
|---|---|---|---|---|---|---|
| | Upper Waldo Canyon Met above Cascade, CO 385449104565501 (P02) | | Waldo Canyon abv Mouth near Manitou Springs, CO 07100750 (QP01) | | Lower Waldo Canyon Met above Manitou, CO 385241104560101 (P01) | |
| **Precipitation (mm)** | | | | | | |
| Time | Instantaneous | Cumulative | Instantaneous | Cumulative | Instantaneous | Cumulative |
| 8/10/2015 11:10 | 0.00 | 0.00 | 0.00 | 0.00 | 0.00 | 0.00 |
| 8/10/2015 11:15 | 0.00 | 0.00 | – | 0.00 | 0.00 | 0.00 |
| 8/10/2015 11:20 | 0.00 | 0.00 | – | 0.00 | 0.00 | 0.00 |
| 8/10/2015 11:25 | 1.02 | 1.02 | – | 0.00 | 0.00 | 0.00 |
| 8/10/2015 11:30 | 0.00 | 1.02 | – | 0.00 | 0.00 | 0.00 |
| 8/10/2015 11:35 | 1.02 | 2.03 | – | 0.00 | 0.00 | 0.00 |
| 8/10/2015 11:40 | 0.00 | 2.03 | 2.03 | 2.03 | 1.02 | 1.02 |
| 8/10/2015 11:45 | 1.02 | 3.05 | 0.00 | 2.03 | 0.00 | 1.02 |
| 8/10/2015 11:50 | 0.76 | 3.81 | 16.00 | 18.03 | 4.06 | 5.08 |
| 8/10/2015 11:55 | 0.00 | – | 2.79 | 20.83 | 2.03 | 7.11 |
| 8/10/2015 12:00 | 0.00 | – | 4.06 | 24.89 | 5.84 | 12.95 |
| 8/10/2015 12:05 | 0.00 | – | 3.30 | 28.19 | 3.05 | 16.00 |
| 8/10/2015 12:10 | 0.00 | – | 0.25 | 28.45 | 0.00 | – |
| 8/10/2015 12:15 | 0.00 | – | 0.00 | – | 0.00 | – |
| Intensity (mm/hr) | – | **7.62** | – | **56.9** | – | **32.00** |

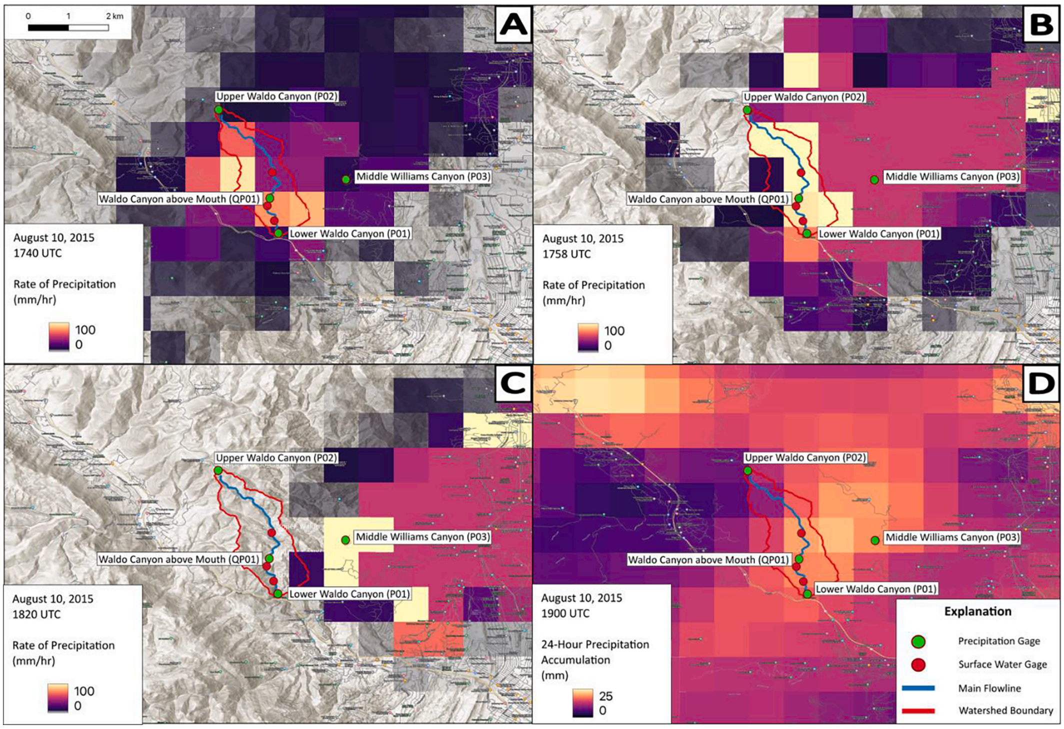

**Fig. 4.** Precipitation estimates from the Multi-Radar Multi-Sensor system when (a) the storm entered Waldo Canyon at 1740 UTC, (b) when peak rainfall rate intensities were reached at 1758 UTC, and (c) when the storm exited the basin at 1820 UTC. Panel (d) shows the radar-estimated rainfall totals for the event. See NOAA NSSL's Multi-Radar Multi-Sensor system (MRMS; NOAA-NSSL, 2023). Precipitation gages (green) are labeled with the station name, surface water radar stations (red) are not labeled. (For interpretation of the references to colour in this figure legend, the reader is referred to the web version of this article.)

Cannon et al., 2008). The second line-of-defense could rely on near-field, real-time velocity and stage radars to validate streamflow in response to extreme precipitation events.

The spatial and temporal distribution of precipitation, the hydrologic response, and the uncertainty analysis associated with the 10 August 2015 event are summarized.

### *4.1. Spatial and temporal distribution of precipitation*

The DEFENS network was operated seasonally during the monsoon season from May through October in 2015 and in 2016; however, only the 2015 data reported significant rainfall and streamflow conditions. Table 3 summarizes the rainfall hyetograph. Fig. 4 illustrates the precipitation distribution from NOAA NSSL's Multi-Radar Multi-Sensor system (MRMS; NOAA-NSSL, 2023). The instantaneous and cumulative precipitation recorded at each rain gage in response to the 10 August 2015 event is illustrated in Figs. 5–7. The event (1) represents the most extreme storm captured during the two-year operation and (2) was highly variable in space and time, which is exhibited by (a) timing in the variability in surface velocity and stage measured at the three radar gages and (b) discrete and cumulative rainfall and intensities recorded at the rain gages.

Rain gage and weather radar data associated with the 10 August 2015 event (Table 3 and Fig. 4) support the contention the storm was

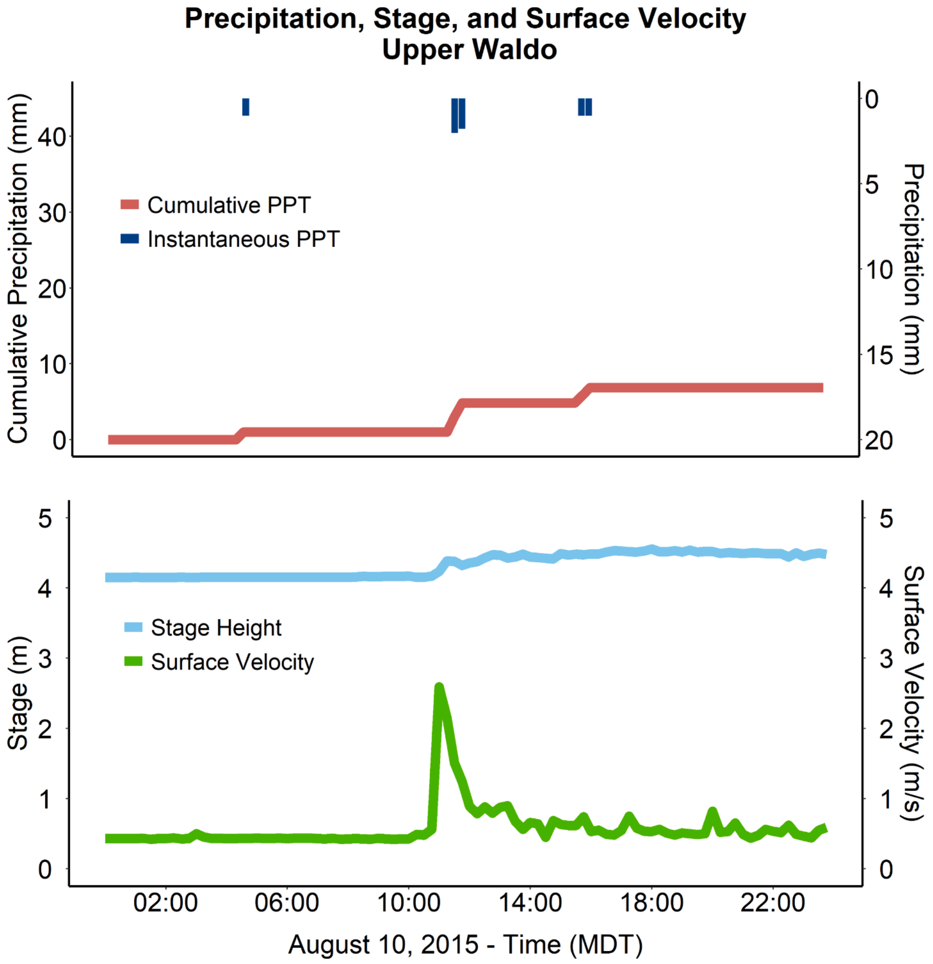

**Fig. 5.** Surface velocity (green) and stage (light blue) recorded at 385344104560601 Waldo Canyon Upper Site near Manitou Springs, Colorado, precipitation (cumulative – red; measured – dark blue) recorded at 385449104565501 Upper Waldo Canyon Met above Cascade, CO, [mm, millimeters; m, meters; m/s, meters per second]. See Fulton and Hall (2024). (For interpretation of the references to colour in this figure legend, the reader is referred to the web version of this article.)

highly variable in space and time. Rainfall intensities reported at rain gages for the Upper Waldo Canyon Met above Cascade, CO, Waldo Canyon above Mouth, and Lower Waldo Canyon Met above Manitou, CO were 7.62 mm/h, 56.9 mm/h, and 32.0 mm/h, respectively, and generally fall within the range of the I-D thresholds (11.6 to 66 mm/h) established by Staley et al. (2015). Precipitation intensities were greatest in the middle part of the basin. Fig. 4 illustrates the evolution of the weather radar rainfall estimates during the 10 August 2015 event. Precipitation began falling in the basin at approximately 1740 UTC (1140 Mountain Daylight Time, MDT) on 10 August and extended through approximately 1820 UTC (1620 MDT).

Precipitation rate estimates from the NOAA MRMS system (available every 2 min at 1 km$^2$ spatial resolution) indicated a weak storm approached the basin from the northwest (Zhang et al., 2016). The storm rapidly intensified directly over Waldo Canyon at 1740 UTC with rainfall covering the entire basin, which corresponded to an instantaneous rainfall rate estimated at 96 mm/h in the upper part of the basin. The entire basin continued to receive rainfall and experienced peak intensities at 1758 UTC with several MRMS pixels estimated at 104 mm/h.

It is worth noting that the radar-based rainfall algorithm operating during this event was the version 11 algorithm described in Zhang et al. (2016). A significant change was implemented later in version 12 for instances where rain is suspected to be mixed with hail (Zhang et al., 2020). In short, version 11 uses a maximum rate threshold (or hail cap) of 104 mm/h; whereas version 12 uses a more sophisticated estimator that enables higher rainfall estimates in such situations. It is thus possible that actual rainfall rates at 1758 UTC were higher than the estimates shown in Fig. 4b given that they were capped at the maximum allowable values. The storm slowly propagated to the east and exited the basin at 1820 UTC. Storm total precipitation amounts from MRMS ranged from 10.3 mm in the upper part of the canyon to 21.4 mm in the southeast part. Fig. 4b indicates the rain gage at Waldo Canyon above Mouth received approximately 30 mm during the event, which further indicates the capped rainfall rates yielded underestimated values over the storm duration.

Little to no precipitation was reported prior to 10 August 2015; however, during the 10 August 2015 event, the heaviest rainfall occurred in the upper part of the basin and quickly translated to surface runoff. This surface runoff traveled downstream and reached the Upper Waldo radar streamgage before it experienced precipitation, which explains the later peak in observed rainfall rates at the site. The Middle Waldo radar streamgage recorded and transmitted a maximum surface velocity of 2.37 m/s and maximum stage of 2.75 m concurrently at 11:15 MDT. The Lower Waldo radar streamgage recorded and transmitted a maximum surface velocity of 3.59 m/s and maximum stage of 2.55 m concurrently at 11:14 MDT. The hydrologic response variables (surface velocity and stage) reached maximum values prior to the maximum rainfall intensities according to rain gages at all three sites.

### 4.2. *Hydrologic response*

The hydrologic response during the 10 August 2015 event is

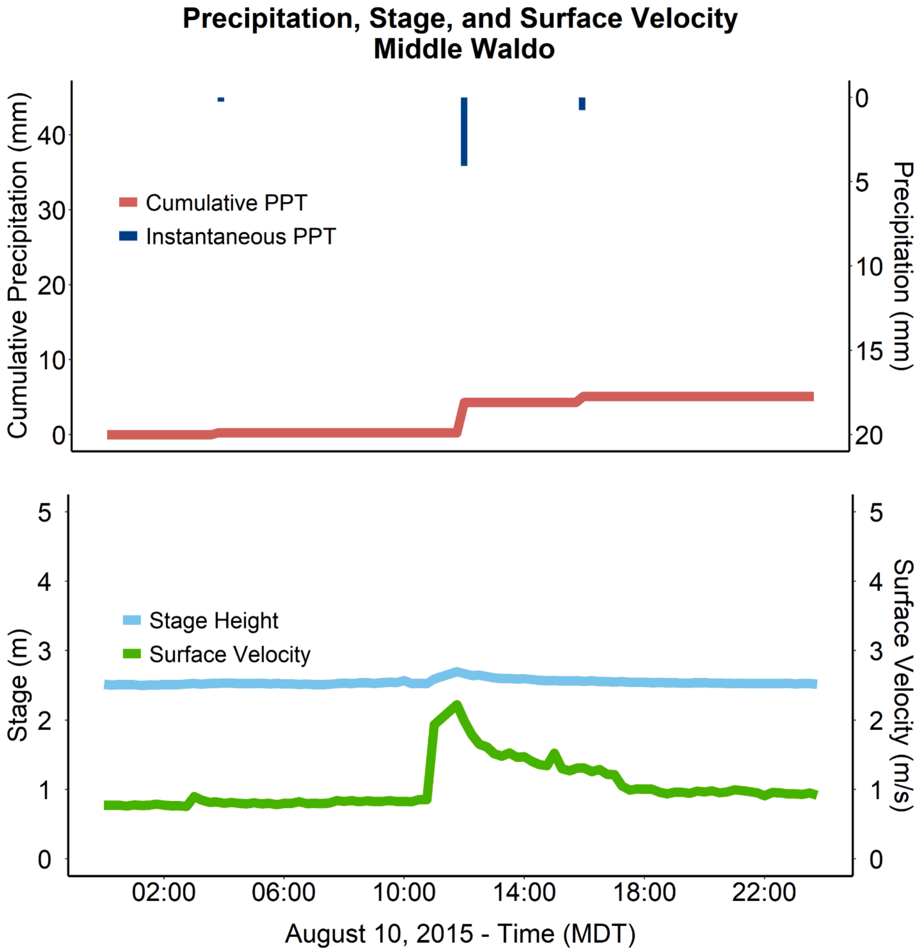

**Fig. 6.** Surface velocity (green) and height (light blue), recorded at 385309104561101 Waldo Canyon Middle Site near Manitou Springs, Colorado, precipitation (cumulative – red; measured – dark blue) recorded at 07100750 Waldo Canyon above Mouth near Manitou Springs, Colorado, [mm, millimeters; m, meters; m/s, meters per second]. See Fulton and Hall (2024). (For interpretation of the references to colour in this figure legend, the reader is referred to the web version of this article.)

illustrated by the surface velocity and stage time-series data (Figs. 5–7) recorded at the Upper Waldo, Middle Waldo, and Lower Waldo radar streamgages. Time series of surface velocity, stage, measurement quality, battery (telemetry and radar), and RSSI were measured and recorded for the 2015 operational period (Fulton and Hall, 2024).

A peak discharge equal to 5.01 $m^3/s$ was computed from a slope-conveyance indirect discharge measurement adjacent to Waldo Canyon above Mouth for the 10 August 2015 event (USGS, 2023b), which is considered an estimate (uncertainty greater than 25 percent). A probability concept-derived peak discharge equal to 4.88 $m^3/s$ validated the indirect discharge measurement proximal to Waldo Canyon above Mouth and is based on a maximum surface velocity, $\phi$, stage, and channel area equal to 2.37 m/s, 0.70, 2.75 m, and 2.94 $m^2$, respectively, recorded by the Middle Waldo radar streamgage. Channel area was derived from a stage-area rating. The probability concept discharge (4.88 $m^3/s$) compares favorably to the indirect measurement (5.01 $m^3/s$), with a percent difference equal to 3.

Discharge time-series was not computed at the three radar streamgages; however, flood wave velocities and travel times were measured and computed at each of the three radar streamgages (Upper Waldo, Middle Waldo, and Lower Waldo). Flood wave velocities varied in response to differences in the at-a-section hydraulic parameters and out-of-bank topography at each site. For example, the flood plains for the Upper Waldo and Middle Waldo radar streamgages are more expansive than the Lower Waldo radar streamgage; the Lower Waldo radar streamgage is installed over an incised channel with a limited flood plain. Assuming a discharge equal to 5.01 $m^3/s$, flood wave velocities for the 10 August 2015 event were computed using the mean kinematic celerity and mean dynamic celerity (downstream component) and were 2.619 m/s ± 0.556 percent and 3.533 m/s ± 0.181 percent, respectively. Validation of predicted flood wave velocities was confirmed using comparisons with measured surface velocities recorded at the Upper Waldo, Middle Waldo, and Lower Waldo radar streamgages (Fig. 8), where maximum-surface velocities during the 10 August 2015 event were 2.9 m/s, 2.37 m/s, and 3.59 m/s, respectively.

Distances from the Upper Waldo, Middle Waldo, and Lower Waldo radar streamgages to U.S. 24 were 2,960 m, 1,460 m, and 644 m, respectively. Flood wave travel times were derived by dividing flow path distances between the radar streamgages and U.S. 24 (Table 2), by the mean values of the kinematic celerity and dynamic celerity. Given the centerline stream distances from the radar streamgages to U.S. 24 (Table 2), flood wave travel times ranged from 19 min to 14 min for the Upper Waldo radar streamgage; 9.3 min to 6.9 min for the Middle Waldo radar streamgage; and 4.1 min to 3.0 min for the Lower Waldo radar streamgage. These timeframes are consistent with the on-site observations made by CDOT personnel during the 10 August 2015 event.

Geomorphic change was documented in the stage record based on the pattern (positive–negative-positive) recorded by the stage radar after the velocity peaked. The channel bed at the Upper Waldo radar streamgage increased in elevation and did not decrease post-event through the end of the radar deployment in October 2015. Geomorphic change did not occur at the Middle Waldo or Lower Waldo radar

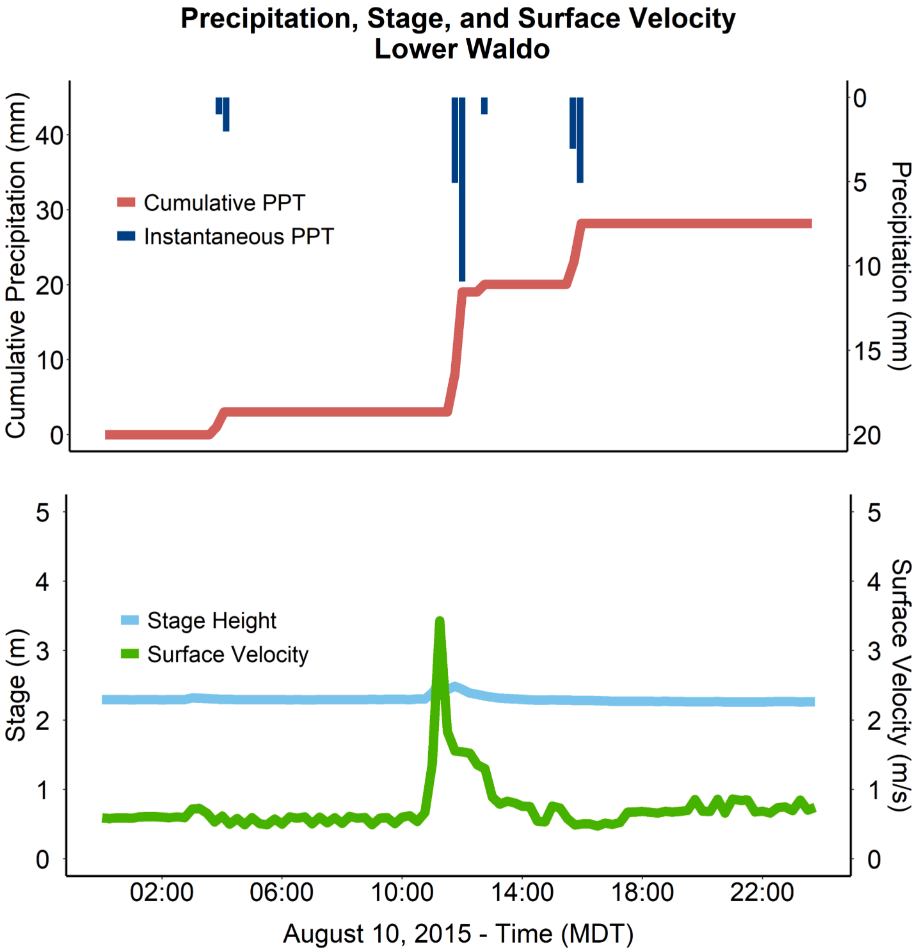

**Fig. 7.** Surface velocity (green) and stage height (light blue), recorded at 385254104560401 Waldo Canyon Lower Site near Manitou Springs, Colorado, precipitation (cumulative – red; recorded – dark blue) measured at 385241104560101 Lower Waldo Canyon Met above Manitou, CO, [mm, millimeters; m, meters; m/s, meters per second]. See Fulton and Hall (2024). (For interpretation of the references to colour in this figure legend, the reader is referred to the web version of this article.)

streamgages and is attributed largely to the non-erodible channel and lack of available sediment source material in the vicinity of the radar streamgage.

### 4.3. Uncertainty analysis

L-moments were (1) computed for a variety of at-section parameters and (2) leveraged to establish their uncertainty and subsequent flood wave velocities and travel times in response to the 10 August 2015 precipitation event. PDFs were selected for each of the three parameters – *slope, hydraulic radius, and depth* – based on the trend and proximity of the 100 subsamples (blue points) to the lines and points on the L-moment plot associated with the PDFs (Fig. 9a, c, and e). The resulting PDFs and CDFs are illustrated in Fig. 9b, d, and f. Distributions incompatible with the raw data, such as the exponential distribution, were not considered.

The distribution of Manning's *n*, similar to the Weisbach resistance coefficient, was assumed to emulate an upper triangular distribution (Ang and Tang, 1990). Slope was best represented by the Generalized Pareto Distribution (GPD) or a lower triangular distribution (Fig. 9A and D). Hydraulic radius (Fig. 9B and E) and depth (Fig. 9C and F) were best represented by the Pearson Type III Distribution (PE3) or normal distribution. For these data, the PE3 distribution is assumed to be equivalent to a normal distribution, which is commonly used to predict the hydrologic variables. Foster (1924) was the first to apply the PE3 distribution to describe the probability distribution of annual maximum flood peaks (Chow et al., 1988). The gravitational constant was represented as a uniform distribution.

The inherent variability and random error in the at-a-section hydraulic parameters associated with physical phenomena as represented by the CV ($\delta = s.d./mean$) and random errors associated with prediction as represented by the CV $\left(\Delta = s.d./mean/\sqrt{no.\ of\ samples}\right)$, respectively, and were computed for the 113 at-a-section values as a function of Manning's *n*, slope, hydraulic depth, depth, and the gravitational constant. The CV for the inherent variability and random error for Manning's *n*, slope, hydraulic radius, depth, and gravitational constant were 0.000, 0.523, 0.180, 0.180 and 0.000 and 0.010, 0.049, 0.017, 0.017,and 0.000, respectively. CVs were derived from the raw data. The total uncertainty in the prediction of mean velocity, kinematic celerity, and dynamic celerity is equal to 0.556, 0.556, and 0.181, respectively. Table 4 summarizes the uncertainties associated with at-a-section hydraulic parameters in Waldo Canyon calculated for the Aug 10, 2015 event.

## 5. Discussion

The study objectives were accomplished by integrating multiple systems (i.e., weather radar, near-field velocity and stage radars, and rain gages) to record flood wave velocities and forecast travel times and communicating the findings.

Weather radar, near-field velocity and stage radars, and rain gages were deployed during portions of 2015 and 2016 to record precipitation and peak discharge events; however, only the 2015 data reported

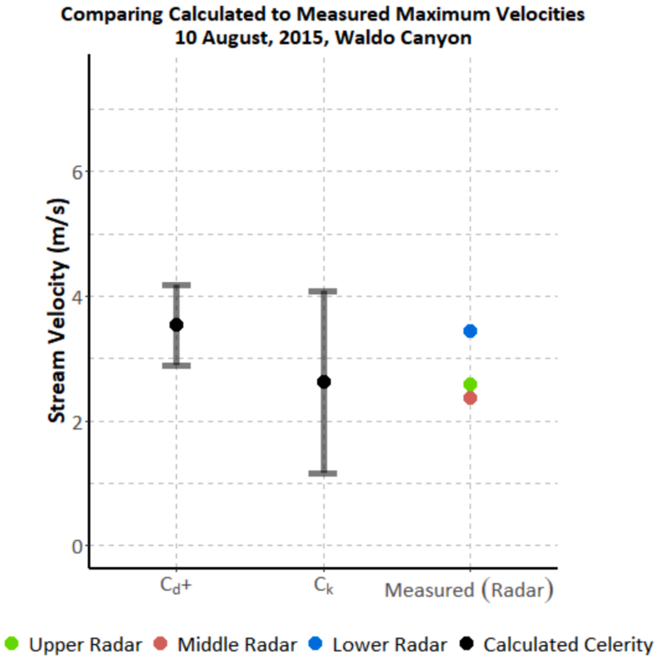

**Fig. 8.** Predicted kinematic celerity and dynamic celerity versus the surface velocity recorded at radar streamgages 385344104560601 Waldo Canyon Upper Site near Manitou Springs, Colorado (Upper Waldo radar), 385309104561101 Waldo Canyon Middle Site near Manitou Springs, Colorado (Middle Waldo radar), 385254104560401 Waldo Canyon Lower Site near Manitou Springs, Colorado (Lower Waldo radar), [meters/sec, meters per second; $c_{d^+}$, downstream flood wave velocity as a function of the dynamic celerity; $c_k$, flood wave velocity as a function of the kinematic celerity]. Mean predicted kinematic celerity and dynamic celerity are represented (black points) along with calculated uncertainties (grey brackets; Table 4). Peak velocity measured at the Upper Waldo (green point), Middle Waldo (red point), and Lower Waldo radar streamgages (blue point) are accompanied by an imposed horizontal line for comparing measured velocity values with calculated celerity values. (For interpretation of the references to colour in this figure legend, the reader is referred to the web version of this article.)

significant rainfall and streamflow conditions. This sensor ensemble highlights the importance of real time data in forecasting and validating storms that generate flash floods. It is evident that a relation exists between the (1) intensity and duration of rainfall, streamflow, and surface velocity and (2) spatial and temporal distribution of rainfall and the timing and magnitude of runoff captured by the surface velocity and stage radars within a basin. The 10 August 2015 event exhibited the greatest rainfall intensity and duration during the deployment period and highlights the importance of the NWS NEXRAD weather radar for advanced warnings, whereas, the USGS sensor ensemble provides a platform for confirming observations from weather radars by delivering the calculated variables flood wave velocities, travel times, and rainfall intensity and duration. The authors did not differentiate between debris flows or flood flows, and the time-series data reflect the raw values that were recorded on the data logger and were not adjusted for outliers or spurious data.

The order of operations to site, install and operate near-field velocity and stage radars and rain gages can be transferred to other post-wildfire basins. Maintenance of stage-area ratings is needed for the probability concept algorithm where radar streamgages are deployed. Slope and cross-sectional elevation profiles would need be re-established to update the flood wave velocity computations prior to any subsequent storms. This necessity is demonstrated by the aggradation in the channel bathymetry recorded after the peak in surface velocity and during the hydrography recession at the Upper Waldo radar streamgage. These data also support the contention that geomorphic change can be tracked using stage radars and is illustrated by the stage-time series in Fig. 5. A peak velocity equal to 2.902 m/s was recorded at the Upper Waldo radar streamgage 11:02 MDT AM. During the recession at 12:15 MDT PM, an increase is river stage was recorded and remained relatively constant until early November when the network was taken offline. This finding also suggests that stage may be less reliable than velocity for detecting rapid changes in streamflow in post-wildfire landscapes where geomorphic changes can interfere with the interpretation of stage data.

The USGS sensor ensemble was integrated with a redundant communication network capable of transmitting surface velocity, stage, and rainfall intensity data in a timely fashion to CDOT and NWS Pueblo WFO staff in advance of impending floodflows. All three radar streamgages recorded a rapid rate-of-change in their respective velocity and stage hydrographs at the onset of the streamflow event. More importantly, the peak surface velocity recorded at the Upper Waldo radar streamgage occurred 103 min earlier than the peak stage. This offset indicates the surface velocity signature from velocity radars may provide longer lead times and advanced warning of impending extreme flows compared to other metrics such as stage and rainfall. Subsequently, the velocity signature could provide decision makers the option to implement corrective action sooner.

At the onset of a precipitation event, representatives from NOAA's NSSL notified the USGS of extreme weather based on weather radar returns. At the same time, the USGS received alarm notifications based on elevated near-field surface velocities derived from the velocity radars. The USGS contacted CDOT to alert them to the event. CDOT representatives arrived on site and confirmed the arrival of a flood wave, which was conveyed safely under U.S. 24 through the re-engineered box culvert. During the rain event, the Upper Waldo radar streamgage recorded and transmitted a maximum-surface velocity of 2.9 m/s at 11:02 MDT AM and a maximum stage of 4.47 m at 12:45 PM MDT – a time difference of approximately 103 min.

Flood forecasting is inherently uncertain. Uncertainties include (1) physical processes, which are random in nature and (2) forecasts or predictions, which lack the forcing data to characterize a physical process (Gourley et al., 2020). Physical processes cannot be controlled; however, a bias-correction factor ($s.d./mean$) can be ascertained from a PDF. The uncertainty associated with physical processes can be established using a central value ($mean$) and a measure of dispersion ($CV$), where observed data are used to estimate the degree of uncertainty. The uncertainty associated with forecasts or predictions can be improved by selecting the appropriate model, acquiring more data, or applying a CV, where uncertainties are characterized by variability in sampling and random errors associated with prediction are represented by a CV (Ang and Tang, 1990). In summary, the physical processes (random) described in Table 4 rely on the mean value ($\bar{x} = mean$) and associated CV ($\delta = s.d./mean$); whereas, forecasts or predictions rely on the random error expressed as a CV $\left(\Delta = s.d./mean/\sqrt{no.\ of\ samples}\right)$.

Given the inherent variability associated with physical phenomenon and random errors, the total uncertainty (Table 4), kinematic celerity uncertainty (0.556), and dynamic celerity uncertainty (0.181) provide a measure of the calculated-flood wave velocities at-a-section in sections of the reach that are not monitored with velocity radars. However, the kinematic celerity returns a higher degree of uncertainty when compared to the dynamic celerity, which offers a better proxy for flood wave velocities (Table 4). Validation of flood wave velocities with uncertainty was confirmed using velocity radars deployed at the Upper Waldo, Middle Waldo, and Lower Waldo radar streamgages, where maximum-surface velocities during the 10 August 2015 event were 2.9 m/s, 2.37 m/s, and 3.59 m/s, respectively (Fig. 8). The surface velocity recorded by the radar streamgages are consistent with the calculated-flood wave velocities.

It should be noted that the flood wave arrival times were approximate and do not consider formal channel routing that accounts for flood plain storage and variations in at-a-section energy dissipation such as

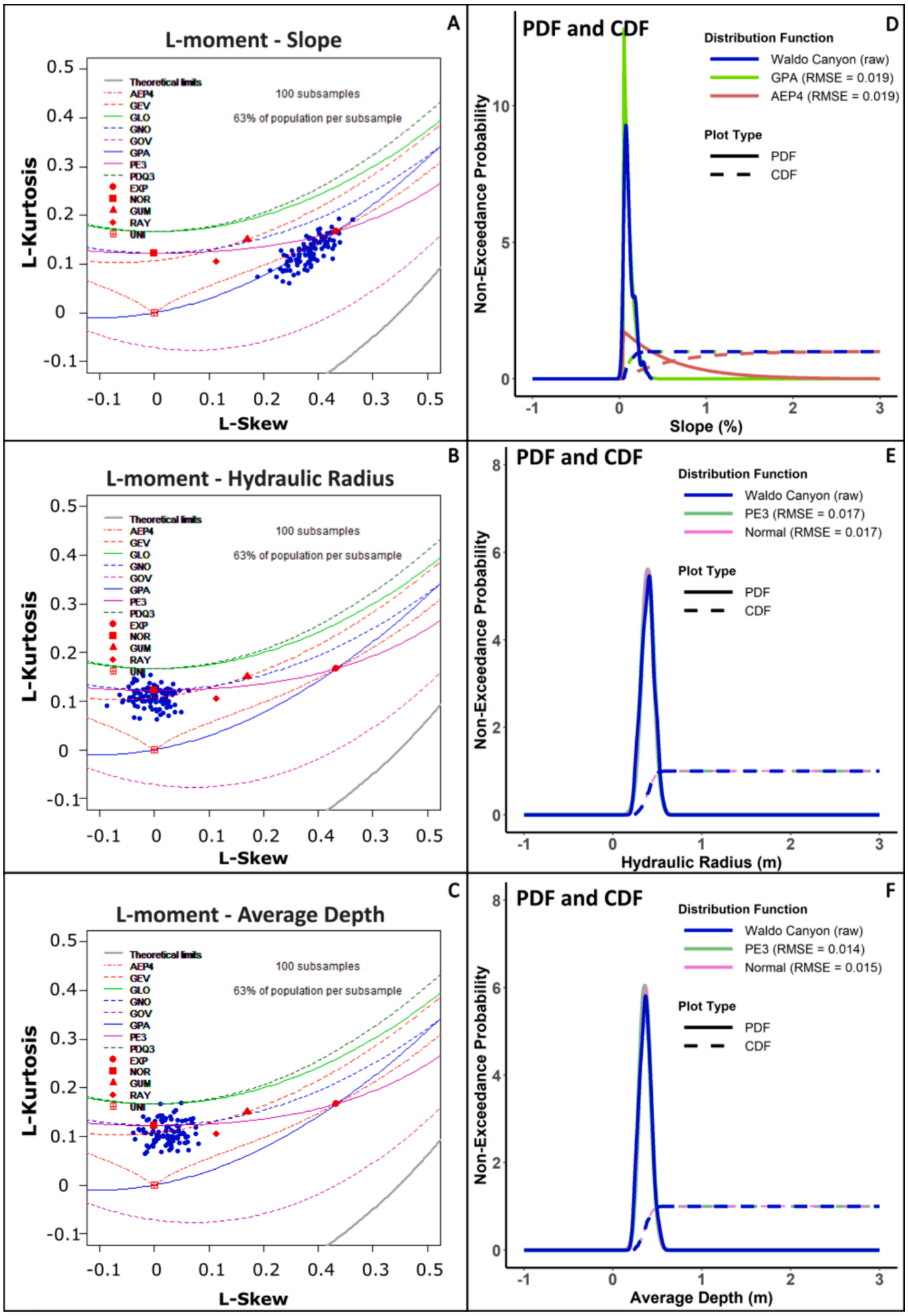

**Fig. 9.** L-moment analysis illustrating the results of 100 subsamples (blue points; A, B, C) collected from the at-a-section slope (A), hydraulic radius (B), and mean channel depth (C) relative to the potential probability distributions: [AEP4, 4-Parameter Asymmetric Exponential Power Distribution, GEV, Generalized Extreme Value Distribution; GLO, Generalized Logistic Distribution; GNO, Generalized Normal Distribution; GOV, Govindarajulu Distribution; GPA, Generalized Pareto Distribution; PE3, Pearson Type III Distribution; PDQ3, Polynomial Density-Quantile3; EXP, Exponential Distribution; NOR, Normal Distribution; GUM, Gumbel Distribution; RAY, Rayleigh Distribution; UNI, Uniform Distribution]. Probability density and cumulative distribution functions were plotted for slope (D), hydraulic radius (E), and mean channel depth (F) for chosen distribution functions and plotted coincidentally with the density curve and empirical cumulative distribution function derived from the raw data (Waldo Canyon). (For interpretation of the references to colour in this figure legend, the reader is referred to the web version of this article.)

Manning's *n* and eddy viscosity terms. In addition, the surface velocity signature illustrated in Fig. 5 peaks earlier in time relative to the stage signature. This is attributed to unsteady flow conditions and variations in water depth and slope. The rate of change in surface velocity serves as surrogate for issuing an advanced warning of potential flood waves.

## 6. Summary and conclusions

In response to extreme post-wildfire precipitation events, near-field Doppler velocity (velocity) and pulsed (stage) radars, rain gages, and a sophisticated communication network were leveraged to compute *a*

**Table 4**

Summary of the uncertainty analysis based on the L-moments generated for the raw at-a-section hydraulic parameters calculated in Waldo Canyon for the 10 August 2015 event, [–, not applicable; m/m, meter per meter; m, meters; m/s, meters per second; $m/s^2$, meters per second squared; m, meters; No. of samples, number of samples; s.d., standard deviation; CV, coefficient of variation].

| Parameter | Distribution | Minimum | Mean | Median | Maximum | No. of samples | s.d. | CV | Inherent variability | Random error | Total uncertainty |
|---|---|---|---|---|---|---|---|---|---|---|---|
| Mean velocity | | | | | | | | | | | |
| Manning's n ($s/m^{1/3}$) | Upper triangular | 0.075 | 0.108 | 0.108 | 0.125 | 113 | 0.000 | 0.109 | 0.000 | 0.010 | |
| Slope (m/m) | Generalized Pareto or lower triangular | 0.029 | 0.112 | 0.094 | 0.322 | 113 | 0.058 | 0.523 | 0.523 | 0.049 | |
| Hydraulic Radius (m) | Pearson Type III or normal | 0.239 | 0.391 | 0.396 | 0.566 | 113 | 0.070 | 0.180 | 0.180 | 0.017 | |
| Mean Velocity (m/s) | – | 0.872 | 1.649 | 1.526 | 3.104 | – | – | – | – | – | 0.556 |
| **Kinematic celerity** | | | | | | | | | | | |
| Manning's n ($s/m^{1/3}$) | Upper triangular | 0.075 | 0.108 | 0.108 | 0.125 | 113 | 0.000 | 0.109 | 0.000 | 0.010 | |
| Slope (m/m) | Generalized Pareto or lower triangular | 0.029 | 0.112 | 0.094 | 0.322 | 113 | 0.058 | 0.523 | 0.523 | 0.049 | |
| Depth (m) | Pearson Type III or normal | 0.226 | 0.364 | 0.364 | 0.541 | 113 | 0.066 | 0.180 | 0.180 | 0.017 | |
| Kinematic Celerity (m/s) | – | 1.402 | 2.619 | 2.405 | 5.023 | – | – | – | – | – | 0.556 |
| **Dynamic celerity** | | | | | | | | | | | |
| Gravitational acceleration ($m/s^2$) | Uniform | 9.754 | 9.754 | 9.754 | 9.754 | 113 | 0.000 | 0.000 | 0.000 | 0.000 | |
| Depth (m) | Pearson Type III or normal | 0.226 | 0.364 | 0.364 | 0.541 | 113 | 0.066 | 0.180 | 0.180 | 0.017 | |
| + Dynamic Celerity (m/s) | – | 2.358 | 3.533 | 3.410 | 5.402 | – | – | – | – | – | 0.181 |

*priori*, measures of surface velocity and stage, rainfall intensity and duration, and transmit in situ debris and flood wave velocities and travel times in Waldo Canyon, Colorado. This sensor ensemble was intended to compliment observations from NWS NEXRAD weather radars and to provide near-field verification of flood wave velocities.

The 10 August 2015 event highlights the importance of weather radar for advanced warnings, velocity and stage radars and rain gages for event validation, and a communication network to deliver notifications to CDOT engineering staff, NWS forecasters, and emergency managers.

The Upper Waldo radar streamgage recorded and transmitted a maximum surface velocity of 2.902 m/s at 11:02 MDT AM and a maximum stage of 4.47 m at 12:45 PM MDT – a time difference of approximately 103 min. The rate-of-change in the surface-velocity signature occurred earlier in time and was greater relative to other metrics such as stage and rainfall, which (1) could provide longer lead times and an advanced warning of impending extreme flows and (2) could allow decision makers the option to implement corrective action.

The kinematic celerity and dynamic celerity served as surrogates for the flood wave velocities. Flood wave travel times were computed using the kinematic celerity and dynamic celerity and were derived by dividing the centerline stream distance from the radar streamgages to U. S. 24. Distances from the Upper Waldo, Middle Waldo, and Lower Waldo radar streamgages to U.S. 24 were 2,960 m, 1,460 m, and 644 m, respectively from U.S. 24. The kinematic celerity and dynamic celerity were validated against the observed maximum-surface velocities at each radar streamgage.

The DEFENS network is both scalable and transferable particularly if other post-wildfire basins (1) exhibit similar hydrologic characteristics to Waldo Canyon and (2) lack site data such as lidar. The L-moment analysis, which includes PDF designations for slope, hydraulic radius, and depth, would be valuable to quickly establish velocity thresholds for an alert network where little or no data on slope, hydraulic radius, or depth exist.

It was demonstrated that the sensor ensemble captured and transmitted flood waves associated with extreme precipitation events and served to validate the weather radar returns provided by NWS WFO. Bathymetric and topographic elevations are needed to derive the independent at-a-section hydraulic parameters (slope, hydraulic radius and depth) required to compute flood wave velocities. Acquiring this information *a priori* would allow more rapid operationalization of an alert network. Collaboration with Emergency Management agencies such as the NWS WFO, who serve as a platform for transmitting alerts allowed timely use of information.

Based on the performance of the sensors and the communication platform, the alert network order of operations to estimate flood wave velocity and travel time could be transferable to other post-wildfire basins where infrastructure and populations could be at risk for flooding. Similarly, the same order of operations could have merit in basins partially burned by wildland fires.

**Supplemental information**

*Time-series Data*

Time series data of stage, surface velocity, data quality, battery telemetry, battery for RQ-30, and Received Signal Strength Indicator is summarized in Fulton and Hall (2024). Data were not scrubbed to remove inconclusive or incomplete data and represents the raw data recorded by dataloggers.

## CRediT authorship contribution statement

**John W. Fulton:** Writing – original draft, Methodology, Funding acquisition, Formal analysis, Conceptualization. **Nick G. Hall:** Writing – original draft, Methodology, Formal analysis. **Laura A. Hempel:** Writing – review & editing, Writing – original draft, Formal analysis. **J.J. Gourley:** Writing – original draft, Formal analysis. **Mark F. Henneberg:** Writing – original draft, Investigation, Conceptualization. **Michael S. Kohn:** Writing – review & editing, Investigation, Formal analysis. **William Famer:** . **William H. Asquith:** Writing – review & editing. **Daniel**

Wasielewski: Investigation. **Andrew S. Stecklein:** Writing – original draft. **Amanullah Mommandi:** Investigation, Conceptualization. **Aziz Khan:** Funding acquisition, Conceptualization.

## Declaration of competing interest

The authors declare the following financial interests/personal relationships which may be considered as potential competing interests: John Fulton reports financial support was provided by US Geological Survey Colorado Water Science Center. John Fulton reports financial support was provided by Colorado Department of Transportation. If there are other authors, they declare that they have no known competing financial interests or personal relationships that could have appeared to influence the work reported in this paper.

## Data availability

A USGS Data Release (Fulton and Hall, 2024; DOI: 10.5066/P981E670) contains the data used in this research and is open access.

## Acknowledgements

This paper and research were supported by the Colorado Department of Transportation and the U.S. Geological Survey. The authors thank Jeannette Oden (USGS) for their editorial review of the manuscript, which improved its readability and Krystal Brown (USGS), Frank Engel (USGS), Paul Steblein (USGS), and the anonymous reviewers for their technical review, and Rob Flynn (USGS) for his supervisor review. Each of these contributions greatly improved the readability and technical merit of the manuscript. The authors would like to thank Peter Ward (Kisters North America, formerly with Hydrologic Services America) and Michael Cook (HyQuest Solutions) for their assistance in parameterizing the near-field radars and data loggers.

Any use of trade, firm, or product names is for descriptive purposes only and does not imply endorsement by the U.S. Government.

## References

Ang, A.H.-S., Tang, W.H., 1990. Probability Concepts in Engineering Design, Volume II Decision, Risk, and Reliability. John Wiley & Sons, New York, New York.

Asquith, W.H., 2011, Distributional analysis with L-moment statistics using the R environment for statistical computing: Createspace Independent Publishing Platform, ISBN 978–146350841—8, Available online: https://www.rdocumentation.org/packages/lmomco/versions/2.4.7/topics/plotlmrdia (accessed on 05 January 2023).

Asquith, W., 2022, lmomco: L-moments, Censored L-Moments, Trimmed L-moments, L-Comoments, and many distributions, Available online: https://cran.r-project.org/web/packages/lmomco/lmomco.pdf (accessed 05 January 2023).

Barthold, F.E., Workoff, T.E., Cosgrove, B.A., Gourley, J.J., Novak, R., Mahoney, K.M., 2015. Improving flash flood forecasts: the HMT-WPC Flash Flood and Intense Rainfall Experiment. Bull. Am. Meteorol. Soc. 96, 1859–1866. https://doi.org/10.1175/BAMS-D-14-00201.1.

Bradley, D.N., 2012, Slope-area computation program graphical user interface 1.0—A preprocessing and postprocessing tool for estimating peak flood discharge using the slope-area method: U.S. Geological Survey Fact Sheet 2012–3112, 4 p.

Cannon, S.H., Gartner, J.E., Wilson, R., Bowers, J., Laber, J., 2008. Storm rainfall conditions for floods and debris flows from recently burned areas in southwestern Colorado and southern California. Geomorphology 96, 250–269.

Cannon, S.H., Boldt, E., Laber, J., Kean, J.W., Staley, D.M., 2011. Rainfall intensity–duration thresholds for postfire debris-flow emergency-response planning. Nat. Hazards 59, 209–236.

Caracena, F., Maddox, R.A., Hoxit, L.R., Chappell, C.F., 1979. Mesoanalysis of the Big Thompson storm. Mon. Weather Rev. 107, 1–17.

Chiu, C.-L., 1987. Entropy and probability concepts in hydraulics. J. Hydraul. Eng. 113 (5), 583–600.

Chiu, C.-L., 1989. Velocity distribution in open channel flow. J. Hydraul. Eng. 115 (5), pp. -594.

Chiu, C.-L., Tung, N.C., Hsu, S.M., Fulton, J.W., 2001. Comparison and assessment of methods of measuring discharge in rivers and streams: Research Report No. CEEWR-4, Dept. of Civil & Environmental Engineering, University of Pittsburgh, Pittsburgh, PA.

Chiu, C.-L., Tung, N.C., 2002. Velocity and regularities in open-channel flow. J. Hydraul. Eng. 128 (4), 390–398.

Chiu, C.-L., Hsu, S.M., Tung, N.C., 2005. Efficient methods of discharge measurements in rivers and streams based on the probability concept: hydrological processes. Wiley Intersci. 19, 3935–3946.

Chiu, C.-L., Hsu, S.-M., 2006. Probabilistic approach to modeling of velocity distributions in fluid flows. J. Hydrol. 316, 28–42.

Chow, V.T., 1959. Open-Channel Hydraulics. McGraw-Hill, p. 680 p..

Chow, V.T., Maidment, D.R., Mays, L.R., 1988. Applied Hydrology. McGraw-Hill Inc, New York, p. 572.

Dalrymple, Tate, and Benson, M.A., 1968, Measurement of peak discharge by the slope-area method: U.S. Geological Survey Techniques of Water-Resources Investigations, book 3, chap. A2, 12 p.

ESRI, 2020. ArcGIS Desktop: Version 10.8.1. Environmental Systems Research Institute, Redlands, CA.

Foster, H.A., 1924. Theoretical frequency curves and their application to engineering problems. Trans. Am. Soc. Civ. Eng. 87, 142–173.

Fritsch, J.M., Carbone, R.E., 2004. Improving quantitative precipitation forecasts in the warm season: a USWRP research and development strategy. Bull. Am. Meteorol. Soc. 85, 955–965.

Fulford, J.M., 1994. User's guide to SAC, a computer program for computing discharge by slope-area method. U.S. Geol. Surv. Open File Rep. 94–360, 31.

Fulton, J.W., Hall, N.G., 2024. Near-field remote sensing of river velocity, stage, and precipitation during portions of 2015 and 2016 in Waldo Canyon, Colorado, USA: U. S. Geological Survey data release. Available online: doi:10.5066/P981E670.

Fulton, J.W., Mason, C.A., Eggleston, J.R., Nicotra, M.J., Chiu, C.-L., Henneberg, M.F., Best, H.R., Cederberg, J.R., Holnbeck, S.R., Lotspeich, R.R., Laveau, C.D., Moramarco, T., Jones, M.E., Gourley, J.J., Wasielewski, D., 2020a Near-field remote sensing of surface velocity and river discharge using radars and the probability concept at 10 U.S. Geological Survey Streamgages. Remote Sens. 12, 1296. 28 p. https://doi.org/10.3390/rs12081296.

Fulton, J.W., Anderson, I.E., Chiu, C.-L., Sommer, W., Adams, J.D., Moramarco, T., Bjerklie, D.M., Fulford, J.M., Sloan, J.L., Best, H.R., Conaway, J.S., Kang, M.J., Kohn, M.S., Nicotra, M.J., and Pulli, J.J., 2020b. Qcam: sUAS-based Doppler radar for measuring river discharge. Remote Sens. 12, 3317. https://doi.org/10.3390/rs12203317.

Fulton, J.W., Ostrowski, J., 2008. Measuring real-time streamflow using emerging technologies: radar, hydroacoustics, and the probability concept. J. Hydrol. 357, 1–10.

Gourley, J.J., Vergara, H., Arthur, A., Clark III, R.A., Staley, D., Fulton, J.W., Hempel, L., Goodrich, D.C., Rowden, K., Robichaud, P.R., 2020. Predicting the floods that follow the flames. Bull. Am. Meteorol. Soc. 101 (7), E1101–E1106. https://doi.org/10.1175/bams-d-20-0040.1.

Jarrett, R.D., 2013, Documentation of the July 1st and 10th, and August 9, 2013 Peak Discharges in the 2012 Waldo Burn Area Streams, prepared August 22, 2013. Available by contacting Bob Jarrett at paleoflood@comcast.net.

Kean, J.W., Staley, D.M., Cannon, S.H., 2011. In situ measurements of postfire debris flows in southern California: comparisons of the timing and magnitude of 24 debris-flow events with rainfall and soil moisture conditions. J. Geophys. Res. 116, F04019.

Kean, J.W., Staley, D.M., Leeper, R.J., Schmidt, K.M., 2012. A low-cost method to measure the timing of post-fire flash floods and debris flows relative to rainfall. Water Resour. Res. 48, W05516.

Kenney, T.A., 2010, Levels at gaging stations: U.S. Geological Survey Techniques and Methods 3-A19, 60 p.

Khan, M.R., Gourley, J.J., Duarte, J.A., Vergara, H., Wasielewski, D., Ayral, P.-A., Fulton, J.W., 2021. Uncertainty in remote sensing of streams using noncontact radars. J. Hydrol. 603 126809. pp. 1-16. Available online: https://doi.org/10.1016/j.jhydrol.2021.126809 (accessed 30 April 2023).

Lancaster, J.T., Swanson, B.J., Lukashov, S.G., Oakley, N.S., Lee, J.B., Spangler, E.R., Hernandez, J.L., Olson, B.P.E., DeFrisco, M.J., Lindsay, D.N., Schwartz, Y.J., McCrea, S.E., Roffers, P.D., Tran, C.M., 2021. Observations and analyses of the 9 January 2018 debris-flow disaster, Santa Barbara County, California. Environ. Eng. Geosci. 27 (1), 3–27. https://doi.org/10.2113/EEG-D-20-00015.

Li. M., Liu, M., Cao, F., Wang, G., Chai, X., Zhang, L., 2022. Application of L-moment method for regional frequency analysis of meteorological drought across the Loess Plateau, China. PloS ONE 17(9): e0273975, Available online: https://doi.org/10.1371/journal.pone.0273975 (accessed 05 January 2023).

Moore, M. and Park, D., 2012, Hydrology Resource Report, Waldo Canyon Fire BAER Assessment – Pikes Peak Ranger District, Pike National Forest, July 17, 2012, Available online: http://cdm15981.contentdm.oclc.org/cdm/singleitem/collection/p15981coll3/id/435 (accessed 27 December 27, 2018).

Moramarco, T., Barbetta, S., Tarpanelli, A., 2017. From surface flow velocity measurements to discharge assessment by the entropy theory. Water (9) 2, 12. Available online: https://doi.org/10.3390/w9020120 (accessed 12 April 2022).

Moramarco, T., Saltalippi, C., Singh, V.P., 2004. Estimation of mean velocity in natural channel based on Chiu's velocity distribution equation. J. Hydrol. Eng. 9 (1), 42–50.

MTBS, 2020, MTBS Glossary: Retrieved from https://www.mtbs.gov/glossary.

NOAA-NSSL, 2023, Multi-Radar Multi-Sensor (MRMS) Operational Product Viewer. Available online: https://mrms.nssl.noaa.gov/ (accessed 10 September 2023).

NOAA-USGS Debris Flow Task Force, 2005, NOAA-USGS debris-flow warning system – Final report: U.S. Geological Survey Circular 1283, 47 p.

R Core Team, 2022. R: A Language and Environment for Statistical Computing. R Foundation for Statistical Computing, Vienna, Austria, Available online: https://www.R-project.org/.

Rydlund, P.H., Jr., and Densmore, B.K., 2012, Methods of practice and guidelines for using survey-grade global navigation satellite systems (GNSS) to establish vertical datum in the United States Geological Survey. U.S. Geological Survey Techniques and Methods, book 11, chap. D1, 102 p. with appendixes, Available online: https://pubs.usgs.gov/tm/11d1/ (accessed on February 3, 2020).

Schumacher, R.S., 2017, Heavy rainfall and flash flooding, Oxford Research Encyclopedia of Natural Hazard Science, Subject: Floods, Convective Storms. DOI: 10.1093/acrefore/9780199389407.013.132.

Staley, D, Gartner, J.E., Kean, J.W., 2015. Objective definition of rainfall intensity-duration thresholds for post-fire flash floods and debris flows in the area burned by the Waldo Canyon Fire, Colorado, USA. 621-624, 10.1007/978-3-319-09057-3_103 in G. Lollino et al. (eds.), Engineering Geology for Society and Territory – Volume 2, doi: 10.1007/978-3-319-09057-3_103, © Springer International Publishing Switzerland 2015.

Staley, D.M., Kean, J.W., Cannon, S.H., Schmidt, K.M., Laber, J.L., 2013. Objective definition of rainfall intensity–duration thresholds for the initiation of post-fire debris flows in southern California. Landslides 10, 547–562.

U.S. Geological Survey (USGS), 2023b. National Water Information System—Web Interface: accessed 10 September 2023. https://nwis.waterdata.usgs.gov/co/nwis/peak?site_no=07100750&agency_cd=USGS&format=rdb.

U.S. Geological Survey, (USGS) 2023a. StreamStats (USGS), Available online: https://www.usgs.gov/streamstats/applications (accessed 18 January 2024).

U.S. Geological Survey, 2021a, USGS water data for the Nation: U.S. Geological Survey National Water Information System database, accessed MONTH DAY, 2021, at https://doi.org/10.5066/F7P55KJN.

U.S. Geological Survey (USGS), 2021b. AreaComp3. Available online: https://www.usgs.gov/software/areacomp-hydroacoustics-software (accessed 06 September 2023).

U.S. Geological Survey, 2021c. Lidar Point Cloud – USGS National Map 3DEP Downloadable Data Collection: U.S. Geological Survey. https://www.usgs.gov/3d-elevation-program.

Verdin, K.L., Dupree, J.A, and Elliott, J.G., 2012, Probability and volume of potential post-wildfire debris flows in the 2012 Waldo Canyon Burn Area near Colorado Springs, Colorado: U.S. Geological Survey Open-File Report 2012–1158, 8 p.

Webb, R.H., Jarrett, R.D., 2002. One-dimensional estimation techniques for discharges of paleofloods and historical floods: Ancient Floods. Modern Hazards: Principles and Applications of Paleoflood Hydrology, AGU's Water Science and Application Series 5, 111–125.

Yochum, S., Bledsoe, B., 2010. Flow resistance estimation in high-gradient streams. In: 4th Federal Interagency Hydrologic Modeling Conference, June 27 – July 1, 2010, Riviera Hotel, Las Vegas, Nevada.

Zhang, J., 2016. Multi-Radar Multi-Sensor (MRMS) quantitative precipitation estimation: initial operating capabilities. Bull. Am. Meteor. Soc. 97, 621–638. https://doi.org/10.1175/BAMS-D-14-00174.1.

Zhang, J., Tang, L., Cocks, S., Zhang, P., Ryzhkov, A., Howard, K., Langston, C., Kaney, B., 2020. A dual-polarization radar synthetic QPE for operations. J. Hydrometeor. 21, 2507–2521. https://doi.org/10.1175/JHM-D-19-0194.1.